MULTIPATH CHANNEL PARAMETER ESTIMATION USING A SWITCHED CIRCULAR ARRAY ANTENNA

by

Nathan Lewis

A thesis submitted in partial fulfillment
of the requirements for the degree

of

MASTER OF SCIENCE

in

Electrical Engineering

Approved:

Dr. George Liang Major Professor	Dr. Jacob Gunther Committee Member
Dr. Randy J. Jost Committee Member	Dr. Byron R. Burnham Dean of Graduate Studies

UTAH STATE UNIVERSITY
Logan, Utah

2006

Abstract

Multipath Channel Parameter Estimation Using a Switched Circular Array Antenna

by

Nathan Lewis, Master of Science

Utah State University, 2006

Major Professor: Dr. George Liang
Department: Electrical and Computer Engineering

This thesis covers the development of a 100 MHz bandwidth wireless channel sounder operating at 2.45 GHz. The spatial and temporal domains of the complex channel impulse response are found by switching between groups of antennas in a 13-element circular array to detect the multiple copies of the transmitted maximal length PN sequence. The well-known maximum likelihood estimation algorithm was adapted for use in finding the angle and time of arrival of each dominant multipath signal. The algorithm is based upon estimating the received signal using a series of calibration measurements. The calibration matrices, consisting of 60 single-signal arrival measurements equally spaced in the azimuth plane, form fundamental basis functions for the received data. The angles and times of arrival of multipath signals are determined by the set of time-delayed calibration matrices that most likely formed the received measurement. Simulations to determine the accuracy of the method were performed. Simple indoor and outdoor measurement data were collected to verify the performance of the sounder.

(84 pages)

To my parents, Dean and Marilee

Acknowledgments

I would like to thank Dr. Liang for his endless patience with me even in the moments when progress was limited or even nonexistent, and for showing confidence in my abilities and the project itself. I'd like to thank Dr. Gunther for his insights and direction when it seemed like all else had failed. Special thanks are due to Dr. Robert D. Tingley at Charles Stark Draper Laboratory, Cambridge, MA, and Dr. Kaveh Pahlavan at the Worcester Polytechnic Institute, Worcester, MA, for the information they contributed in regards to the development and implementation of the calibration based maximum likelihood method used in this thesis. Finally, I'd like to thank Jared Bench for all his help, late night hours spent making measurements, positive hard-working attitude, and for the crazy Irish music.

Nathan Lewis

Contents

Page

Abstract . . . . . **iii**

Acknowledgments . . . . . **v**

List of Tables . . . . . **viii**

List of Figures . . . . . **ix**

Acronyms . . . . . **xii**

1 Introduction **1**
1.1 Channel Sounder Comparisons 2
1.2 Previous Measurements by Others 4

2 Channel Model **6**
2.1 Model Based on the Ideal Array Steering Vector 8
2.2 Physical Array Model Based on Calibration Matrices 10
2.2.1 Array Calibration Matrices 10
2.2.2 Received Signal Strength 12
2.3 Maximum-Likelihood Estimation 12

3 Channel Sounder **15**
3.1 Transmitter 15
3.2 Receiver 19
3.2.1 Array Antenna 20
3.2.2 Oscilloscope 21
3.3 Calibration Measurements 26
3.3.1 Calibration Procedure 26
3.3.2 Calibrated Power 27
3.3.3 Array Mutual Coupling and Shadowing Effects 28
3.4 Data Processing 28

4 MLE Simulations **35**
4.1 Noiseless Simulations 35
4.1.1 Angular Resolution 35
4.1.2 Temporal Resolution 37
4.1.3 Conclusions for Simulations without Noise 39
4.2 Direction of Arrival Simulations with Noise 39
4.3 Algorithm Efficiency 41

5 Measurement Results **46**
5.1 Calibration Test Measurements 46
5.2 Calibration Improvements 48
5.3 LOS Measurements Along a Hallway 51
5.4 NLOS Measurements Along a Hallway 53
5.5 NLOS Measurements 56

6 Conclusion **62**

References **65**

Appendix **67**

List of Tables

Table Page
3.1 Transmitter components. 16
3.2 Receiver components. 20
3.3 Oscilloscope initialization parameters. 23
4.1 Iterative parameter estimation for AOAs of 0 and 30 degrees. 37
4.2 Iterative parameter estimation for TOAs 0 and 12 ns. 38
4.3 Signal parameters for the noisy simulations. 41
5.1 Parameter estimates for receiver location RX1. 53
5.2 Parameter estimates for receiver location 1 in ENGR. 56
6.1 A possible bank arangement improvement. 64

List of Figures

Figure Page

2.1 Wireless multipath channel. 7

2.2 2D wireless multipath ray model. 8

2.3 Plane wave impinging on array of M Sensors. 11

3.1 Picture of transmitter. 16

3.2 Transmitter block diagram. 16

3.3 Power spectral density showing signal spreading. 18

3.4 Time domain resolution. 18

3.5 Picture of receiver. 19

3.6 Receiver block diagram. 20

3.7 Receiver array. 22

3.8 Picture of receive array. 22

3.9 Oscilloscope data acquisition. 24

3.10 Switch and trigger timing. 25

3.11 Location of calibration measurements. 25

3.12 Phase variation over subsequent PN sequences. 27

3.13 Ideal magnitude and phase response. 29

3.14 Actual magnitude and phase response. 29

3.15 Signal down conversion and alignment. 30

3.16 Time alignment of reference signals using correlation with PN code. 31

3.17 Phase alignment of reference signals using correlation with PN code. 31

3.18 Time aligned reference signals. 32

3.19 Phase aligned reference signals. 32

3.20 Signal subspace created by calibration basis functions. 34

4.1 First order cost function for a single arrival at zero degrees. 36

4.2 First order cost function for AOAs of 0 degrees and 30 degrees. 36

4.3 Cost function for two signals separated by 12 ns. 38
4.4 Multipath parameter estimates for an SNR of 30 dB after 8 iterations. . . . 40
4.5 Multipath parameter estimates for an SNR of 30 dB after 5 iterations. . . . 40
4.6 Multipath parameter estimates for an SNR of 0 dB. 42
4.7 Multipath parameter estimates for an SNR of -10 dB. 42
4.8 Average of 20 snapshots with an SNR of -10 dB. 43
5.1 Parameter estimates for calibration test measurement after 1 iteration. . . . 47
5.2 Parameter estimates for calibration test measurement after 20 iterations. . . 47
5.3 Phase comparison for outdoor measurement. 48
5.4 Parameter estimates for an AOA of 3 degrees after 2 iterations. 49
5.5 Parameter estimates for an AOA of 3 degrees after 20 iterations. 49
5.6 Phase comparison for repeat calibration. 50
5.7 Locations of transmitter and receiver for LOS hallway measurements. . . . 52
5.8 Hallway signal parameter estimates for position RX1. 52
5.9 Parameter estimates correlated with actual paths. 53
5.10 Locations of 4^{th} floor diffraction measurements. 54
5.11 4^{th} floor LOS measurement 1. 54
5.12 4^{th} floor NLOS measurement 2. 55
5.13 4^{th} floor NLOS measurement 3. 57
5.14 4^{th} floor NLOS measurement 4. 57
5.15 4^{th} floor NLOS measurement 5. 58
5.16 Locations of EL NLOS classroom measurements. 59
5.17 Classroom-to-classroom propagation (Position 1). 59
5.18 Classroom-to-hallway propagation (Position 2). 60
5.19 Classroom-to-hallway propagation (Position 3). 60
A.1 EL second floor hallway measurement distances. 68
A.2 Picture from location P1. 69
A.3 ENGR fourth floor measurement distances. 69

A.4 Picture from location P2. 70
A.5 Picture from location P3. 70
A.6 EL second floor classroom measurement distances. 71
A.7 Picture from location P4. 71
A.8 Picture from location P5. 72

Acronyms

AOA	angle of arrival
BPSK	binary phase-shift key
BS	base station
CIR	channel impulse response
DOA	direction of arrival
EC	Engineering Classroom building
EL	Engineering Lab building
ENGR	Engineering building
LOS	line-of-sight
MIMO	multiple-input-multiple-output
ML	maximum likelihood
MLE	maximum-likelihood estimation
MS	mobile station
NLOS	non-line-of-sight
RF	radio frequency
SAGE	space-alternating generalized expectation-maximization
SER	Science and Engineering Research building
SDMA	space division multiple access
SNR	signal-to-noise ratio
TOA	time of arrival
UCA	uniform circular array
ULA	uniform linear array

Chapter 1

Introduction

Efficient design of modern high speed wireless networks requires detailed understanding of the wireless channel and how signals propagate across it. The ground and objects, such as buildings and trees, near the transmitter or receiver create multiple paths (multipaths) for the signal to arrive at the receiver. The signal propagates from the transmitter along different paths and arrives at the receiver with different time delays and from different directions. Thus, the received power is spread in both temporal and spatial domains. Each multipath signal can be characterized by its amplitude, time delay, and angle of arrival (AOA).

Recent research has led to new methods to improve the capacity of today's networks that exploit the multipath nature of the channel. Smart antennas improve the signal-to-noise ratio (SNR) by using beamforming along with sophisticated signal processing algorithms to determine the directions of the desired signal and interfering sources. The main lobe of the antenna is then placed in the direction of the desired signal and the nulls of the radiation pattern are placed in the directions of the interferers. Space division multiple access (SDMA) has been proposed as a new access scheme utilizing smart antennas that allow multiple signals to be distinguished from each other based on their AOA, thus increasing system capacity. Multiple-input-multiple-output (MIMO) systems use multiple antennas at the transmitter and receiver to profit from spatial diversity. It has been shown that MIMO systems can significantly increase the capacity of a system in a highly cluttered environment [1].

The purpose of this thesis is twofold: to develop a channel sounder capable of resolving multipath signals in indoor and outdoor environments, and to measure individual signal arrivals in order to determine their respective mulipath components. To accomplish the

first goal, a channel sounder that employs an omnidirectional antenna at the transmitter and a switched uniform circular array (UCA) antenna at the receiver will be developed. The sounding signal will be a 2.45 GHz carrier that is BPSK modulated by a 511-bit m-sequence PN-code with 100 MHz bandwidth. The modulated RF signal will be sampled at the receiver by a 4-channel Tektronix digital phosphor oscilloscope and stored for digital post-processing. A super-resolution direction of arrival (DOA) algorithm that estimates the multipath signal components will be implemented.

Simple indoor and outdoor measurements will be made with an attempt to trace the paths taken by the dominant received signals. A comprehensive analysis will be performed to correlate the measurements with the physical properties of wave propagation such as reflection, diffraction, and scattering of the signal from objects in the physical environment. A statistical analysis of the multipath delays, AOAs, and received signal strength will be performed to classify different environment types.

1.1 Channel Sounder Comparisons

A number of channel sounders that measure the complex channel impulse response (CIR) in either the temporal or spatial domain or both, have previously been developed by other researchers [2–5]. The temporal CIR is measured by using an appropriate sounding signal: a wideband pulse, a maximal length PN code, or a frequency swept chirp signal [6]. It has been shown that the temporal effects of the channel can be determined equally well by using either a PN-code or a frequency swept chirp [7], while a wideband pulse is more susceptible to interference from other sources operating in the same frequency band. The spatial properties of the channel are measured by mechanically rotating a highly directive antenna [8], [9], or by using a synthetic aperture array [2], [10] or physical array [3], [4], along with a super-resolution direction of arrival (DOA) algorithm. Directional antennas are advantageous because there is no need for angular domain processing. Synthetic arrays and directive antennas both have the advantages that only one receiver channel is needed, have no mutual coupling effects, and are usually more cost-effective than a multiple channel physical array. Both types of antennas, however, require highly precise control of the

antenna position or orientation, that for directive antennas at lower frequencies becomes impractical. Physical arrays have the advantage of simultaneously sampled channels and no moving parts, but can be quite costly and require extensive array calibration to mitigate the effects of mutual coupling between array elements.

Due to the absence of a precise positioning system, a physical array antenna will be used. Array geometry effects the angular resolution and the choice of a suitable DOA algorithm. Signals arriving from any direction in the azimuth plane can be distinguished from one another by using a rectangular or circular planar array. Circular arrays are an attractive choice due to their uniform resolving capabilities in the azimuth plane.

Super-resolution DOA algorithms such as ESPRIT [2], MUSIC [11], and SAGE [12], are based on the far-field model of ideal arrays where the magnitude of each element is identical to that of every other element and the phase is modeled by the time delay of the impinging signal. Because of mutual coupling that exists when physical arrays are used, this model fails to accurately represent the received signal. Furthermore, when using a planar array, the magnitude response of the elements opposite to the source bearing direction will be greatly attenuated due to the signal being blocked by other elements. By including array mutual coupling effects into the signal model, standard DOA algorithms such as MUSIC and ESPRIT can be used [13]. However, in order to account for element shadowing effects, calibration measurements consisting of a single arrival must be made for as many angles as possible. A convienient way to incorporate calibration data into the signal model has been proposed [3] and utilizes the maximum likelihood (ML) principle to find the AOA and TOA of multipath signals. The model was developed for data that is collected using a frequency domain channel sounder, but is adapted in this thesis for a time domain channel sounder. Although the method is quite computationally complex relative to MUSIC, ESPRIT, and SAGE, it is conveniently based on the calibration data that is necessary to account for mutual coupling, shadowing effects, slight deviations from omnidirectional radiation patterns, array imperfections, and differences in the magnitude and phase response of RF ciruitry in each channel. Besides being computationally complex,

the model is also based on the accuracy of the calibration measurements and the assumption that coupling effects are the same in all environments, which is not always true.

1.2 Previous Measurements by Others

The majority of channel sounding experiments previously performed have been carried out to characterize certain channel types by 1) statistically analyzing the spatial and temporal dispersion effects of the channel, 2) to verify the capabilities of a specific channel sounder or direction of arrival (DOA) algorithm, 3) to trace all dominant paths from transmitter to receiver in an attempt to understand propagation mechanisms, or 4) a combination of the above. Urban macrocellular measurement campaigns [2], [10], [14], [15] are reported where the measurements were made with the base station (BS) placed at or above the average rooftop level and the mobile station (MS) at street level. Measurements were made at both the BS [10] and the MS [2] [15]. The dominant waveguiding effect of streets was confirmed in each case. In general the total received power is shown to arrive in specific "clusters" in time and space [10]. A comparison of different types of "propagation classes" is made by determining the percentage of power at the receiver arriving from each cluster. Path tracing has been attempted in outdoor urban channels by utilizing double-directional channel measurements where AOA data from both ends of the link have been made [14].

In addition to urban channel characterization, many microcellular and picocellular (indoor) measurements have been made [3], [5], [8], [9], [16–18]. A propagation case where both transmitter and receiver are located on the rooftop of a three story building surrounded on three sides by higher buildings was studied to determine the reflection properties of exterior building walls [5]. By tracing the signals arriving at the receiver, it was shown that exterior building walls contribute specular reflection along with some spatial spreading. Other measurements have been performed with the purpose of statistically analyzing the effects of indoor channels [8], [9], [17]. Durgin et al. [17] provide statistical parameters for signals at 2.4 GHz for indoor-indoor, outdoor-indoor, outdoor-outdoor, and floor-floor propagation on campus at Virginia Tech, but made no attempts to geometrically trace the paths from transmitter to receiver. However, Xu et al. used the same channel sounder at 60 GHz in an

attempt to geometrically trace indoor-indoor propagation paths [8]. Results showing the reflective properties of wall materials, the waveguiding effect of hallways, and the dispersion effects of metallic studs in walls, along with statistics relevant to each measurement case are included. Barbot et al. [18] provide measurement results at 2.2 GHz for an outdoor transmitter and indoor receiver where one or two dominant paths are traced in each measurement location.

The remainder of this thesis will be organized as follows. Chapter 2 will present the multipath channel model to accurately represent the transmitted and received signals. Chapter 3 will describe our experimental setup along with its characteristics, limitations, and calibration issues. In Chapter 4, the measurement concept will be simulated in order to determine the expected behavior of the system. Chapter 5 will report and analyze the measurement results. A summary along with ideas for future measurements and research will be provided in Chapter 6 to conclude the work.

Chapter 2

Channel Model

Wireless systems designers rely on channel models to predict parameters such as received power, mean excess delay, rms delay spread, excess delay spread, etc. These parameters influence the system's power, bit rate, and bandwidth requirements and influence hardware specifications.

Channel models that predict the effects of the channel on the transmitted signal are highly dependent on the signal of interest. Classical models that predict the received power and variations of signal amplitude as functions of position and time are usually sufficient for narrow band signals. On the other hand, wideband signals require additional information regarding the time dispersion of the channel. Furthermore, adaptive antennas, SDMA systems, and MIMO channels require additional information regarding the spatial properties of the channel.

Signal propagation for all terrestrial wireless systems is multipath in nature. Objects in the channel cause the transmitted waves to reflect, diffract, or scatter especially for NLOS propagation. Multiple copies of the signal arrive at the receiver with different time delays, amplitudes, phases, and AOAs. The fields at the receiver are superposed such that the received signal is a summation of all the multipath components of the transmitted signal. The received signal can thus be modeled as a summation of time-shifted, phase-shifted, scaled versions of the original transmitted signal.

An example of a typical multipath channel is illustrated in fig. 2.1. As shown the path length and therefore the propagation delay, amplitude, and phase varies for each incoming signal. The amplitude and phase of each signal is further affected by the reflection and diffraction coefficients of the objects it encounters.

If all reflections, diffractions, and scattering occur in the far field of the receiver the

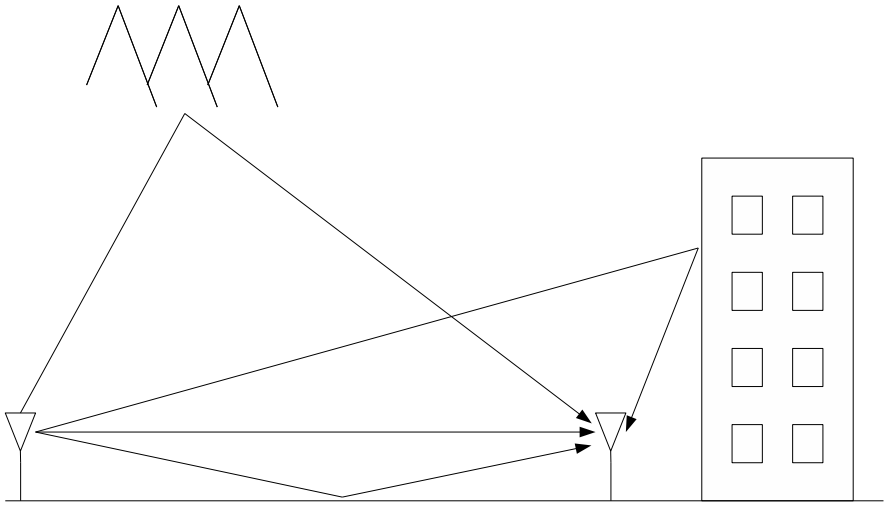

Fig. 2.1: Wireless multipath channel.

impinging waves can be approximated as plane waves that are represented as "rays" impinging on the receiver. Figure 2.2 shows an example of a 2D outdoor multipath channel showing the dominant rays arriving at the receiver. Assuming that the transmit and receive antenna heights are the same, each ray shown consists of two rays, one in the horizontal plane connecting the transmitter and receiver and one that is reflected off the ground.

If the transmitted signal is an RF carrier that is BPSK modulated by a maximal length PN-code (m-sequence), it can be written as

$$x(t) = u(t)cos(2\pi f_c t) \tag{2.1}$$

where $u(t)$ is the chosen m-sequence that assumes values of ± 1. The sounding sequence $u(t)$ is a periodic signal with period, T, such that

$$u(t) = u(t - T). \tag{2.2}$$

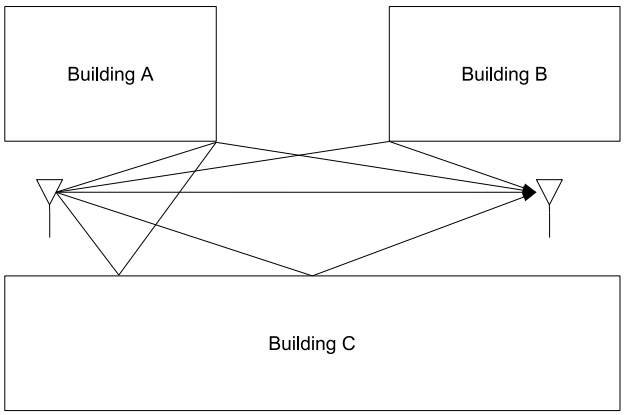

Fig. 2.2: 2D wireless multipath ray model.

Assuming that the receiver consists of an array of K antennas, the received signal at a reference point, **O**, chosen to be the center of the array, is given by

$$y(t) = \sum_{l=1}^{L} \alpha_l u(t - \tau_l) cos(2\pi f_c t - \Phi_l) \tag{2.3}$$

where α_l, τ_l, Φ_l are the complex amplitude, time delay, and phase of the l^{th} multipath component, respectively, and L is the number of dominant multipath signals needed to accurately estimate the received signal. The complex baseband signal is formed from the output of the down-converted in-phase and quadrature-phase receiver branches such that

$$R_{bb}(t) = R_I(t) + jR_Q(t) \tag{2.4}$$

where $R_I(t)$ and $R_Q(t)$ are respectively the demodulated in-phase and quadrature-phase signal components. The demodulated signal at the reference point, **O**, is then

$$y(t) = \sum_{l=1}^{L} \alpha_l u(t - \tau_l) e^{j\Phi_l}. \tag{2.5}$$

2.1 Model Based on the Ideal Array Steering Vector

The use of an ideal array antenna at the receiver provides the ability to determine the

AOAs of the incoming signals by comparing the phases of each signal on each antenna in the array. The signal model is based on the assumption that 1) the signals all arrive in the azimuth plane, 2) the signals sources are all in the far-field of the array, and 3) the inverse signal bandwith is much larger that the largest dimension of the array divided by the speed of light. Figure 2.3 shows a signal impinging on a planar array of K sensors. The gray lines show the wavefronts of constant phase impinging on the reference point, **O**, which is located at the center of the array. The position of the k^{th} sensor in the array can be written as the vector $\mathbf{r_k}$ whose tail is at **O** and points to the location of the k^{th} sensor, while the AOA of each impinging wave can be represented by the unit vector $\mathbf{e}(\phi)$, which points in the direction of the incoming signal. By assuming zero phase at the reference point, the phase on the k^{th} element of the array is given by

$$\Phi_k = e^{j\frac{2\pi}{\lambda}\langle \mathbf{e}(\phi), \mathbf{r_k} \rangle} \tag{2.6}$$

where λ is the carrier wavelength and $\langle \cdot, \cdot \rangle$ is the inner product of two vectors. The steering vector, $c(\phi)$, which contains the phase of each element of the array is given by

$$c(\phi) = \begin{bmatrix} e^{j\frac{2\pi}{\lambda}\langle \mathbf{e}(\phi), \mathbf{r_1} \rangle} \\ e^{j\frac{2\pi}{\lambda}\langle \mathbf{e}(\phi), \mathbf{r_2} \rangle} \\ \vdots \\ e^{j\frac{2\pi}{\lambda}\langle \mathbf{e}(\phi), \mathbf{r_K} \rangle} \end{bmatrix}. \tag{2.7}$$

The received signal matrix can now be modeled as

$$Y(t) = \begin{bmatrix} y_1(t) \\ y_2(t) \\ \vdots \\ y_K(t) \end{bmatrix} = \sum_{l=1}^{L} \alpha_l c(\phi_l) u(t - \tau_l) + N(t) \tag{2.8}$$

where $N(t)$ is a vector of the complex noise processes for each receiver channel.

2.2 Physical Array Model Based on Calibration Matrices

The signal model presented in eq. (2.8) is useful to represent the measurements made by an ideal array antenna, and in the development of DOA algorithms MUSIC, ESPRIT, and SAGE. However, the use of a physical array severely limits its accuracy. Mutual coupling between antenna elements complicates the model since the phase on each element is also effected by neighboring antennas and is not simply a function of antenna position and the AOA of the signal. Furthermore, when using a 2D physical array, one element can block or shadow the power received by another element. For example, when using a circular array, an element located on the positive x-axis will block the power received by an element on the negative x-axis if the signal arrives at zero degrees azimuth. Array calibration that accounts for both the coupling and shadowing effects is essential. Most previous direction finding experiments have been accomplished by moving a single element to different positions thus creating a synthetic array that is free of mutual coupling and shadowing. If a physical array is indeed used instead of a sythetic array, the model presented in eq. (2.8) becomes inadequate. Mutual coupling is assumed to be independent of the AOA of the impinging signals and can therefore be accounted for by including a signal transformation using a mutual coupling matrix [13]. However, since the shadowing effects are different for each AOA, standard DOA algorithms such as SAGE, MUSIC, and ESPRIT lead to inaccurate parameter estimation.

A new model has been proposed [3] that combines array calibration with the maximum likelihood principle to find the AOA and TOA of multipath signals.

2.2.1 Array Calibration Matrices

All channel sounders require array calibration to account for any inaccuracy of element positioning, mutual coupling, or magnitude and phase differences of the RF components in each receiver chain. The shadowing effect present for 2D arrays can also be mitigated if the array response is measured for all AOAs of interest. The baseband calibration data for

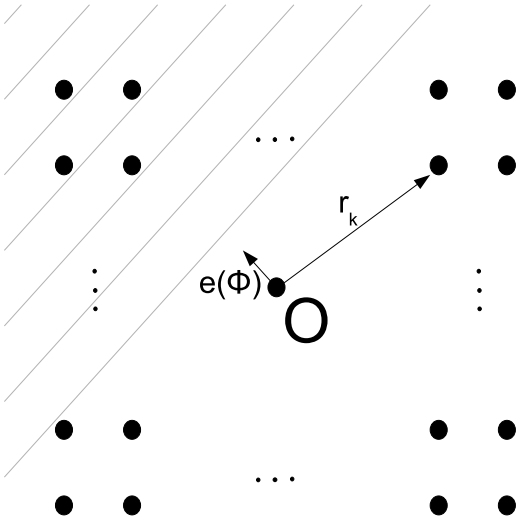

Fig. 2.3: Plane wave impinging on array of M Sensors.

each discrete AOA is arranged in matrix form as

$$U_m = \begin{bmatrix} u_{1,1} & u_{1,2} & \cdots & u_{1,K} \\ u_{2,1} & u_{2,2} & & \\ \vdots & & \ddots & \\ u_{\eta,1} & & & u_{\eta,K} \end{bmatrix} \tag{2.9}$$

where the row indices represent consecutive time samples, the columns represent each antenna element, K is the number of antennas in the array, and η is the number of samples required to capture one period of the sounding sequence. It follows that

$$\eta = T \cdot f_s \tag{2.10}$$

where f_s is the sampling frequency of the receiver and T is the sequence period. Calibration matrices are created for m=1,2,...,M, where M is the number of discrete AOAs measured.

Using the array calibration matrices from eq. (2.9), the new received signal matrix becomes

$$Y = \sum_{l=1}^{L} \alpha_l U(n_l; \phi_l) + N \tag{2.11}$$

where $U(n_l;\phi_l)$ is created by time-shifting the calibration matrix that corresponds to an AOA of ϕ_l by n_l time samples. In eq. (2.11), N is an $\eta \times K$ noise matrix whose values N_{ij} are normally distributed with zero mean and standard deviation σ^2 and are statistically independent of N_{kl} provided that $i \neq k$ and $j \neq l$.

2.2.2 Received Signal Strength

The formation of the signal model in terms of scaled, time-shifted versions of the calibration matrices provides a convenient method for determining the power of the incoming signals. Since power is proportional to signal amplitude squared it is only necessary to calculate the power received for each calibration matrix. Since all calibration measurements are made sequentially at the same transmitter to receiver separation, the power received for calibration matrix U_m is equal to the power received for calibration matrix U_n. Given the calibration power, P_c, the power of the lth multipath parameter, P_l, is

$$P_l = |\alpha_l|^2 P_c \tag{2.12}$$

for P_c given in units of mW. In decibels eq. (2.12) is given as

$$P_l(dBm) = 20log(|\alpha_l|) + P_c(dBm). \tag{2.13}$$

2.3 Maximum-Likelihood Estimation

Maximum-likelihood estimation (MLE) [19] is the process by which the probability that a random variable X assumes a particular value V is maximized by varying a parameter θ upon which X depends. In the present case of estimating the multipath channel parameters, the random variable of interest is the channel snapshot or measurement matrix V and $\theta^L = [\alpha, n, \phi]$ are the multipath signal parameters, where α, n, and ϕ are $L \times 1$ vectors containing the complex amplitude, discrete time delay, and AOA estimates, respectively. The superscript L is used to denote the model order (the number of paths to be estimated).

Given the model for the received signal matrix in eq. (2.11) the likelihood function given by

$$p(V|\theta^L) = p_V\left(V - \sum_{l=1}^{L} \alpha_l U(n_l;\phi_l)\right) \tag{2.14}$$

where $p(V|\theta^L)$ is the conditional probability of the received signal matrix, V, given the signal parameters, θ^L.

To solve the maximum likelihood estimation, $M \times N$ basis functions U_{mn} are formed by time-delaying each calibration matrix U_m for $m = 1, \ldots, M$ by $n = 0, \ldots, N-1$ discrete delays. The likelihood function in eq. (2.14) can be expressed as

$$p(V|\theta^L) = \frac{e^{-X}}{det(\pi\sigma^2 I)} \tag{2.15}$$

where

$$X = \|V - \sum_{l=1}^{L} \alpha_l U(n_l;\phi_l)\|_F^2 \tag{2.16}$$

and $\|\cdot\|_F$ denotes the Frobenius norm. The estimated values $\hat{\theta^L}$ are those for which the squared Frobenius norm of the difference between the measured data and the measurement model is minimized.

According to the model in eq. (2.11), L values of α, n, and ϕ are needed to accurately represent the measured results. A parallel search for the L values of $\hat{\theta^L}$ over all angles; $m = 1, \ldots, M$; and all delays; $n = 0, \ldots, N-1$; that minimize X according to eq. (2.16) would require $(M \times N)^L$ function evaluations [3]. As the number of incoming paths increases, the computational complexity of the parallel search becomes impractical.

Instead of implementing a full parallel search, a recursive serial search [3] is used. This method is implemented by searching first for a single arrival, and then iteratively incrementing the model order until all L paths have been found. The i^{th} iteration assumes a model order of i. The parameters $\hat{\theta}^{i-1}$ that minimized the previous iteration are fixed while the i^{th} path parameters are found by searching all times and angles remaining from the previous iteration. The new recursive serial search requires $M \times N \times L$ function evaluations

where the function assumes the order of the number or paths found at that iteration. Additional detail on data handling, processing and implementation will be given in the following chapter.

Chapter 3

Channel Sounder

A channel sounder capable of measuring multipath channel in indoor and outdoor propagation environments has been designed and built for this work and future wireless channel research at Utah State University. The sounder transmits and receives a 100 MHz BPSK modulated signal at the ISM band of 2.45 GHz. The modulating signal is a maximal length pseudo-random noise (PN) code consisting of 511 bits with a chip duration of 20 ns. The multipath components of the transmitted signal incident on the receive antenna array are sampled and stored for off-line digital processing. The signal parameters are estimated from the received data using the maximum-likelihood principle outlined in Chapter 2.

3.1 Transmitter

A photograph of the equipment setup and schematic of the transmitter are shown in fig. 3.1 and fig. 3.2, respectively. The transmitter consists of an RF frequency synthesizer, a progammable arbitrary waveform generator used to generate the PN sequence, an RF mixer, an adjustable power amplifier capable of transmitting at 23 dBm, and an 8.5 dBi omnidirectional transmitting antenna with 15 degrees vertical beamwidth. For the calibration measurements a parabolic antenna with 19 dBi gain, 12 degrees horizontal beamwidth, and a front to back ratio of 25 dB was used. A rubidium reference standard was used to phase lock the RF synthesizer and PN-code generator. Table 3.1 lists the transmitter components, the manufacturer, and part number.

As previously noted the sounding signal used in this experiment was a 511-bit maximal length PN sequence. With the use of the arbitrary waveform generator a PN sequence of any length can be programmed and downloaded to the waveform generator. The chip rate,

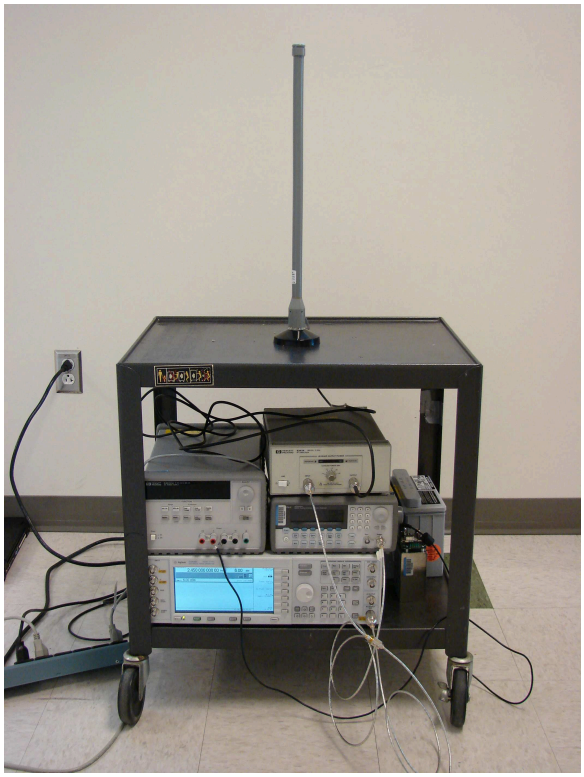

Fig. 3.1: Picture of transmitter.

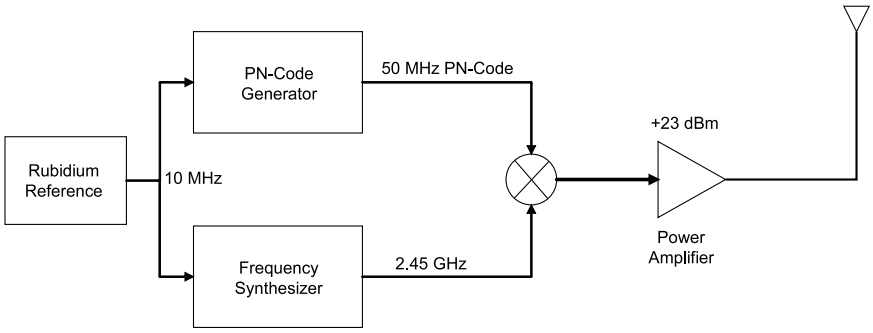

Fig. 3.2: Transmitter block diagram.

Table 3.1: Transmitter components.

Component	Manufacturer	Part #
Arbitrary Waveform Generator	Agilent	33250A
Frequency Synthesizer	Agilent	E4438C
Power Amplifier	Agilent	8347A
RF Mixer	Mini-Circuits	ZXO5-30W
Rubidium Reference	Stanford Research Systems	PRS10
Omni Antenna	Hyperlink Technologies	HG2409U
Parabolic Antenna	Hyperlink Technologies	HG2419G

R_c, is determined by setting the sequence repetition rate according to

$$R_c = \frac{N}{T} \tag{3.1}$$

where $1/T$ is the sequence repetition rate and N is the sequence length. The main lobe bandwidth of a PN sequence is determined by

$$BW = 2R_c. \tag{3.2}$$

Since the desired bandwidth for the sounder was 100 MHz, a 50 MHz sequence was downloaded to the waveform generator by setting the sequence repetition rate to 97.874 kHz. The resulting sequence period was 10.22 μs.

PN codes, often called spreading codes, are used as channel sounding signals because of their inherent interference rejection capabilities, and their autocorrelation properties in the time domain. The term spreading is used when the code is mixed with with a signal that results in "spreading" the signal's power across a wider bandwidth. To demonstrate the wider bandwidth, measurements were made with both the transmitted carrier and the mixed signal which were sampled directly by the oscilloscope. Figure 3.3 shows the power spectral density of the narrowband carrier and the wideband PN modulated signal.

Multiple signals arriving at the receiver with different time delays can be distinguished by correlating the received signal with a copy of the transmitted PN sequence. The autocorrelation of a PN code is given by

$$R_{uu}(\tau) = \int u(t+\tau)u^*(t)dt \tag{3.3}$$

where τ is the signal delay variable. Correlating the received signal with a copy of the transmitted PN sequence will create peaks in the time domain that correspond to the delay of the each incoming signal. The width of each peak is twice the chip duration, or $2/R_c$ (40 ns in the present case). If two signals arrive within 40 ns of each other, their peaks begin to overlap but remain discernible as long as the arrival time separation is greater than

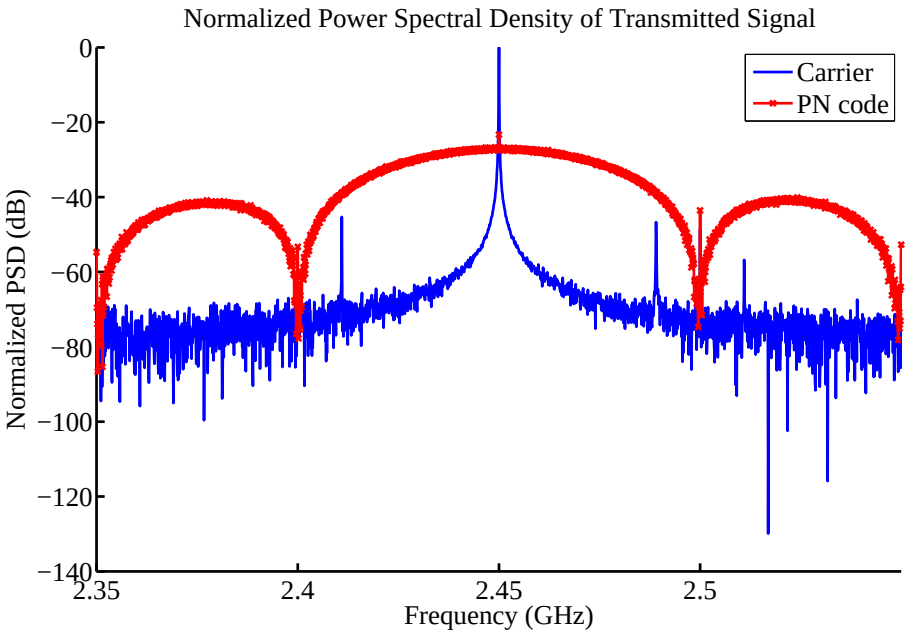

Fig. 3.3: Power spectral density showing signal spreading.

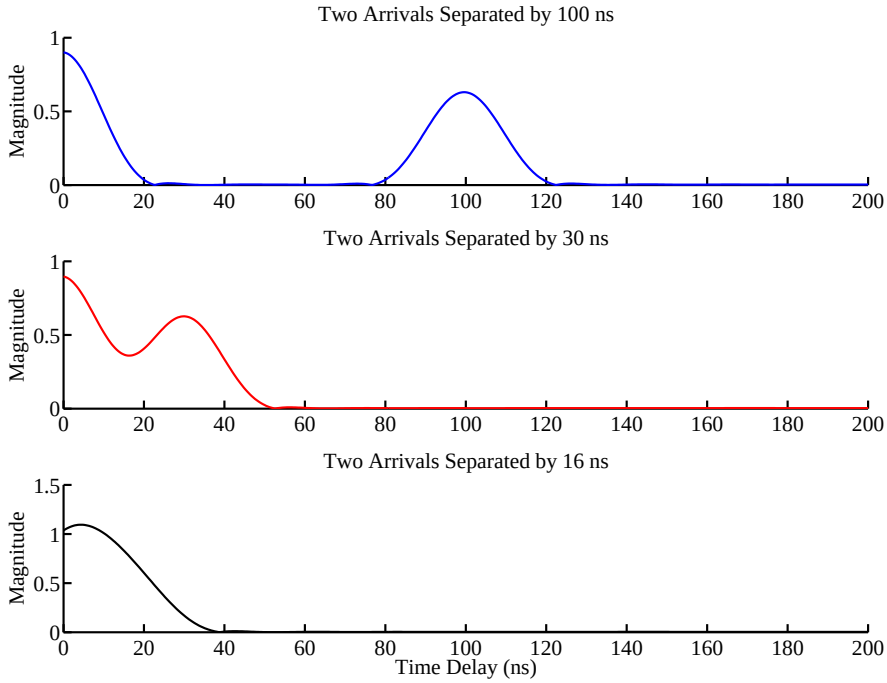

Fig. 3.4: Time domain resolution.

approximately $1/R_c$ or 20 ns. The temporal resolution of a time domain channel sounder is thus $1/R_c$ or equivalently, $2/BW$. An example of two signals arriving with time delay separation of 100 ns, 30 ns, and 16 ns is given in fig. 3.4.

3.2 Receiver

A photograph of the equipment setup and schematic of the receiver are shown in fig. 3.5 and fig. 3.6, respectively. The receiver consists of an array of 13 elements, three four-channel RF switches to switch between 12 array elements, four low noise amplifiers, four 100 MHz bandpass filters, and a four-channel oscilloscope used to sample the received signal. The oscilloscope accepts a standard rubidium reference clock to phase lock the sampling rate to the carrier frequency. A custom made switch control unit controls the position of each switch and also provides a trigger signal to the oscilloscope. Table 3.2 lists the receiver components, the manufacturer, part number, specified gains, and bandwidth.

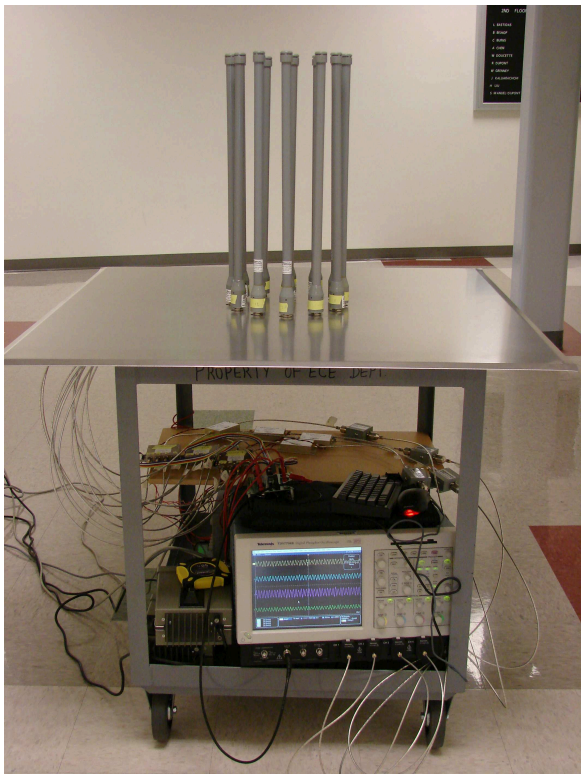

Fig. 3.5: Picture of receiver.

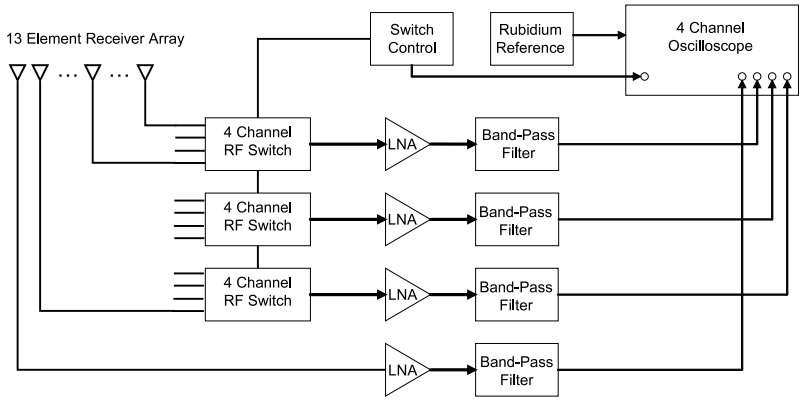

Fig. 3.6: Receiver block diagram.

Table 3.2: Receiver components.

Component	Manufacturer	Part #	Gain	Bandwidth
Oscilloscope	Tektronix	TDS7704B	Adjustable	0-7 GHz
Band Pass Filter	Teletronics	BPF2450	-3 dB	2400-2500 MHz
Low Noise Amplifier	Mini-Circuits	ZRL-2400LN	25 dB	1900-2400 MHz
4-Channel Switch	JFW	50S-1173	-4 dB	800-3000 MHz
Omni Antenna	Hyperlink Technologies	HG2409U	8.5 dBi	2400-2500 MHz

3.2.1 Array Antenna

Two types of arrays were considered for the measurement apparatus: uniform linear array (ULA), and uniform circular array (UCA). The number of elements, and the array geometry effect the angular resolution of the array. For an array of any geometry, the total number of signals that can be simultaneously detected is equal to $K-1$, where K is the number of elements used. An array's ability to resolve closely spaced signals increases as the maximum dimension of the array increases, as long as the far-field approximation given by

$$R > \frac{2D}{\lambda} \tag{3.4}$$

where R is the source to receiving antenna separation, still holds. Furthermore, to neglect the signal time delay between elements of the array, the largest dimension of the array, D,

must be much smaller than the speed of light divided by the signal bandwidth, or

$$D \ll \frac{c}{BW}. \tag{3.5}$$

Although the ULA geometry maximizes the largest array dimension, D, and therefore has the best angular resolution, it also has major drawbacks in that it is able to measure only half of the azimuthal plane, and the resolution is not uniform over all angles. Due to the front-to-back ambiguity of a linear array, a back plane must be used to block all signals that are reflected from objects behind the array. The modified antenna radiation pattern due to the back plane must be included in the received signal model. Any deviations from a flat plane or small displacement of the back plane relative to the array will change the radiation pattern of the elements. Although an ULA maximizes the angular resolution, it does so only at angles near antenna boresight. As the angles of arrival deviate from antenna boresight the received signal power along with the resolving capabilities of the array are drasctically reduced.

On the other hand, an UCA has less angular resolution than an ULA with an equal number of elements, but has uniform resolution over all angles and does not require consideration of the element radation pattern. The receive antenna array that was used for the measurements in this work is composed of 13 antenna elements. The elements are arranged with 12 elements equally spaced with an inter-element spacing of $\lambda/2$, and one element at the center of the circle used as the reference element, as shown in fig. 3.7. A close-up picture of the receive array is given in fig. 3.8.

3.2.2 Oscilloscope

As shown in fig. 3.6, the receiver consists of four channels, three of which are used to switch between antenna elements 1 through 12, where the elements are numbered as shown in fig. 3.7. The remaining channel is reserved for making reference antenna measurements. The signal on each channel is ampilified and filtered and then sampled by a four-channel, pc-based oscilloscope capable of sampling up to 20 GSa/s, and storing up to four million

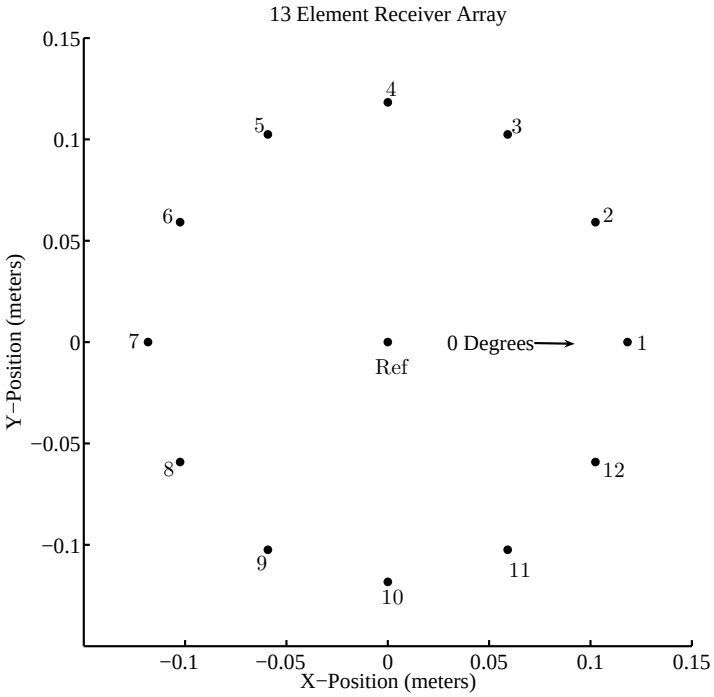

Fig. 3.7: Receiver array.

Fig. 3.8: Picture of receive array.

Table 3.3: Oscilloscope initialization parameters.

Parameter	Value
Sample Rate per Channel	2.5 GSa/s
Record Length per Channel	100,000
Trigger Mode	Normal External
Channels	1-4
Verticle Scale	Various

data points. When configured to sample all four channels, the per channel sampling rate is one-fourth the overall sampling rate, resulting in a maximum per channel sampling rate of 5 GSa/s. Each channel of the oscilloscope is equipped with an adustable gain amplifier that is set by changing the y-axis scale, followed by an 8-bit A/D converter. For each measurement the y-axis scale was set just larger than the received signal amplitude to maximize the A/D converter resolution.

To capture data from a 13 element array using a four-channel oscilloscope, the receive array was divided into four banks of antennas. Bank one, corresponding to switch position one, contained the reference antenna and elements one through three; bank two, corresponding to switch position two, contained the reference antenna and elements four through six; and so on. The sampling scheme used by the oscilloscope and the timing of the switch control unit are outlined in fig. 3.9 and fig. 3.10, respectively. Data acquisition was automated in a MATLAB script that made use of the TekVISA software provided with the oscilloscope. Before any data could be collected data acquisition parameters such as trigger mode, sampling frequency, record length, number of channels to sample, and the verticle scale were sent to the oscilloscope. The initialization parameters used in all the measurements are given in table 3.3.

The oscilloscope is queried for the trigger reference time after initialization. When a new trigger reference time is detected the data stored in channels 1 through 4 of the oscilloscope are saved to the system memory. A count variable is then incremented, and the program again queries for the reference time until a new trigger was detected. After the count reaches four, all four banks have been sampled and the data from each channel along with a record of the trigger reference time and initialization parameters are saved to

the hard drive for off-line processing.

A simple microcontroller was used to control the switches and the timing of the oscilloscope trigger signal. An infinite loop of switch and delay commands was programmed to the microcontroller and is shown in fig. 3.10. When the trigger signal is in a logic low state, the switches are toggled to the next incremental switch position. Since the switch time is specified to be 20 μs, a delay of 100 μs is inserted before setting the trigger signal to a logic high. After a new trigger signal is detected by the data acquisition program, an average of three seconds are needed to save the data to system memory. Four seconds after the trigger is set, the switch is again toggled to the next position. After switch position 4, corresponding to bank four, a five second delay is inserted. By examining the saved trigger reference times, the data corresponding to bank one can be identified as the data following the five second delay.

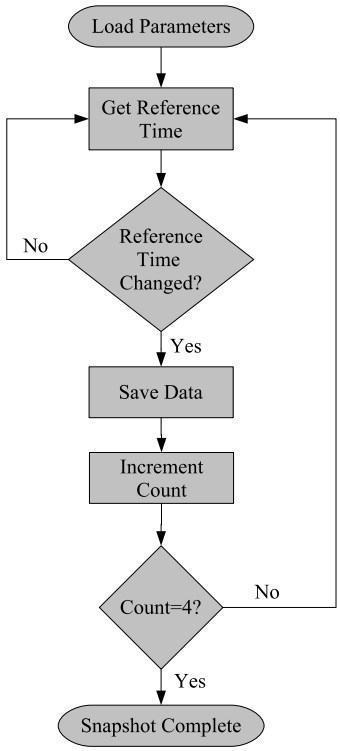

Fig. 3.9: Oscilloscope data acquisition.

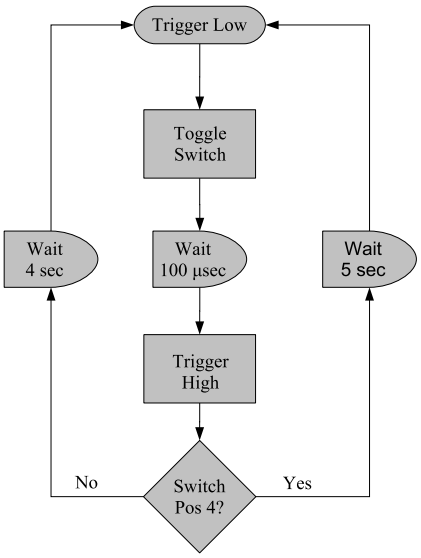

Fig. 3.10: Switch and trigger timing.

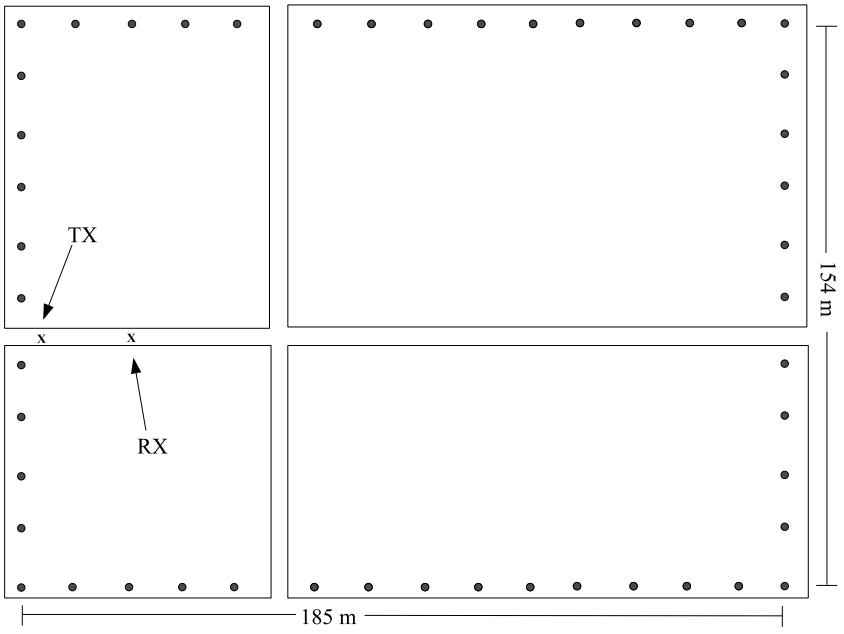

Fig. 3.11: Location of calibration measurements.

3.3 Calibration Measurements

Calibration measurements that form the basis of the received signal model outlined in Chapter 2 were made in an open field on the USU campus shown in fig. 3.11. The circles mark the approximate location of the trees that line the perimeter of the field. Two perpendicular sidewalks partition the field into uneven quadrants as shown in fig. 3.11. The measurements were made on a calm evening, from 8:00 pm to 10:30 pm, when no people or moving objects were on the field. The ambient temperature was reported as 74 degrees Fahrenheit. The transmitter made use of a 19 dBi parabolic antenna with 12 degree beamwidth and 25 dB front to back ratio to minimize any signal power transmitted behind the transmitter and to the sides. The antenna was pointed directly towards the receiver 10 meters away. Any reflected signal from the main beam of the antenna would have to travel 258 meters farther than the direct line of sight path. Using the free space propagation model, the reflected signals are attenuated by at least 28 dB. According to the manufacturer's specifications, the strongest side-lobe of the radiation pattern occurs at ± 30 degrees and is attenuated by 20 dB. Hence, any reflections from the antenna side lobes are assumed to be negligible compared to those originating from the main beam. The calibration measurements used in a previous experiment [3] were made in an anechoic chamber where any reflected signal was attenuated by 30 dB.

3.3.1 Calibration Procedure

Since no automatic positioning system was available, the calibration measurements were made by manually rotating the receiver cart. The array was first oriented with zero degrees facing the transmitter. The measurement consisted of collecting 125,000 samples per channel at a rate of 1.25 GSa/s, resulting in 9 PN sequence periods. Figure 3.12 shows the variation of the phase calculated from each of the nine PN sequences. The standard deviation of the phase angle calculated from 40 calibration measurements each consisting of nine PN sequences was 3.38 degrees. The standard deviation of the magnitude variations for the same measurements was 0.22%. To minimize the effect of noise, each of the nine PN sequence periods were averaged to determine the most accurate phase response.

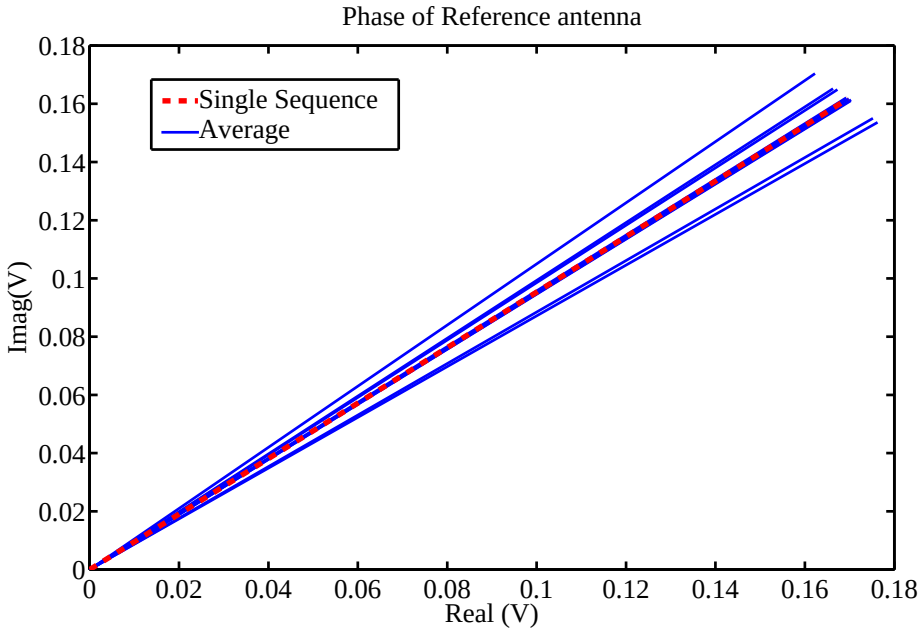

Fig. 3.12: Phase variation over subsequent PN sequences.

After a single measurement was made, the array was manually rotated by aligning the corners of the cart with markings equally spaced every six degrees on a foam board template. The absolute accuracy of the zero degree measurement is assumed to be about one degree. The estimated accuracy of the array rotations is less than half a degree. The calibration matrices U_m for $m = 1, \ldots, 60$ were formed from the calibration measurements.

3.3.2 Calibrated Power

As stated in Chapter 2, the power of the incoming signals is determined by multiplying the received calibration power by the magnitude squared of the incoming mutlipath component. Using the transmit power, antenna gain, and free space path loss, the power of the signal at the receiver can be approximated by the well-known Friis Transmission Equation

$$P_r(dB) = P_t(dB) + G_t + 20 * log\left(\frac{\lambda}{4\pi R}\right) \tag{3.6}$$

where $P_r(dBm)$ and $P_t(dBm)$ are the power at the receiver and transmitter, respectively, G_t is the transmit antenna gain in dBi, λ is the signal wavelength, and R is the transmitter

to receiver separation. For a calibration transmit power of +23 dBm, a transmit antenna gain of 19 dBi, a wavelength of 12.24 cm, and a transmitter to receiver separation of 10 m, the power at the reciever is -18.23 dBm. For the remainder of this work the received calibration power, P_c is assumed to be -18.23 dBm.

3.3.3 Array Mutual Coupling and Shadowing Effects

As previously discussed, mutual coupling and signal shadowing caused by the use of a physical circular array must be modeled in order to use algorithms that are based on ideal array responses. Unfortunately, existing methods to account for mutual coupling are AOA independent and therefore cannot account for the AOA dependent shadowing effects. To demonstrate mutual coupling and element shadowing the ideal and measured magnitude and phase response of antenna 1 for all 60 calibration measurements are shown in fig. 3.13 and fig. 3.14, respectively. Since the same receiver channel was used for all 60 measurements the irregular amplitude and phase values shown in fig. 3.14 are a function of only the AOA of the calibration signal. These array imperfections can be modeled by measuring the array response for all AOAs of interest. The calibration based MLE algorithm presented in Chapter 2 is able to determine the signal parameters by deterimining the calibration matrices that most likely caused the measured signal to occur.

3.4 Data Processing

Since the data model in eq. (2.11) is based on data received from each element simultaneously, the measured channel data must be modified so as to be equivalent to sampling all 12 channels simultaneously. Figure 3.15 shows how the data is downconverted and modified to represent simultaneously sampled data. The sampled RF data from bank κ for $\kappa = 1, \ldots, 4$; is multiplied by sine and cosine functions. The double frequency components are removed by low-pass filtering the data. It follows that the complex received signal is $R_I + jR_Q$. Since more than one period of the PN sequence was sampled, the data is averaged over consecutive sequence periods, so that the total data length is equal to the length of one PN sequence. After averaging the data, the reference antenna signal is correlated with

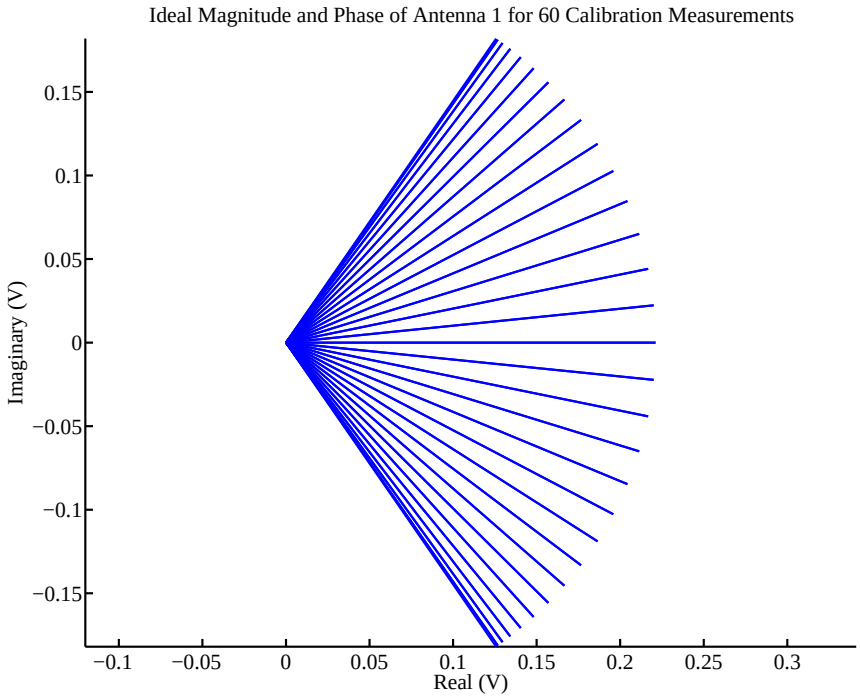

Fig. 3.13: Ideal magnitude and phase response.

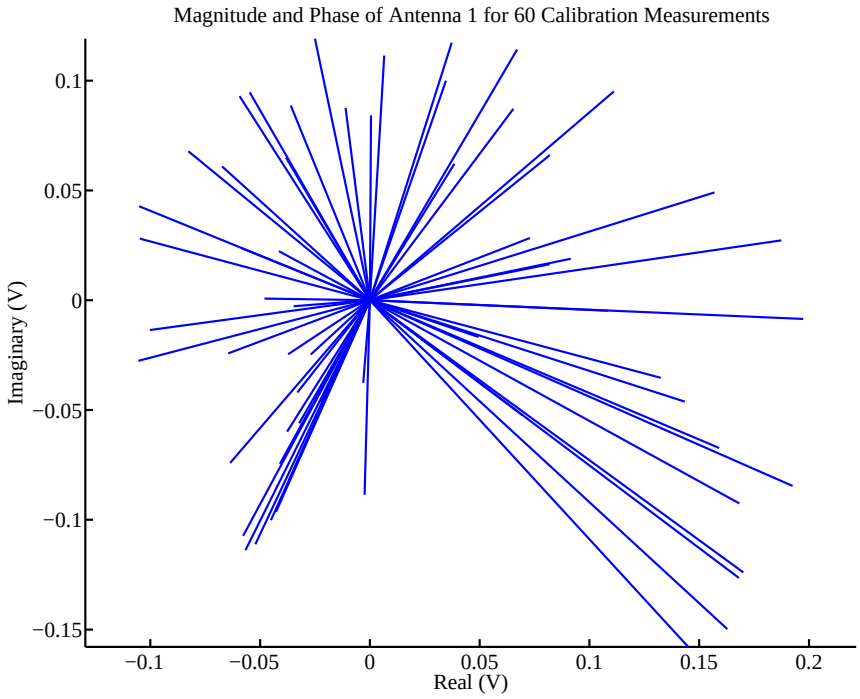

Fig. 3.14: Actual magnitude and phase response.

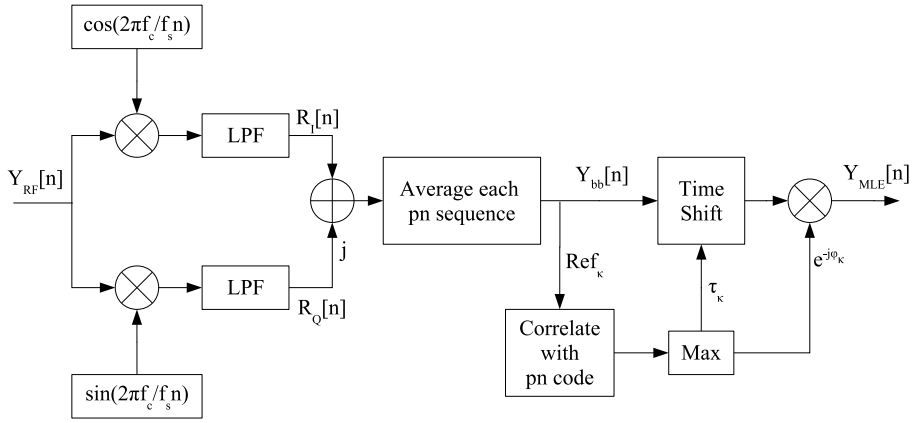

Fig. 3.15: Signal down conversion and alignment.

a copy of the transmitted PN sequence. Figure 3.16 and fig. 3.17 show the magnitude and phase of the correlated signal for a typical indoor LOS measurement. Since the timing of the trigger signal is accurate to only a few microseconds, the time delay and phase of the reference antenna will be random. The time delay, τ_κ, and the phase, ϕ_κ, are found for the largest received signal. Each bank is then phase-shifted so that the phase of each reference signal equals zero. Since there is no absolute time reference, for LOS measurements, each bank is time-shifted so that largest signal arrives at a delay corresponding to propagation time along the LOS path. Since the strongest signal is not necessarily the first signal for NLOS measurements, each bank is time-shifted so that the largest signal arrives at a time delay of 120 ns. The final step is to downsample the data by a factor of 10 to minimize the algorithm processing time. The resulting equivalent sampling rate is 250 MHz. Figure 3.18 and fig. 3.19 show the time and phase aligned reference signals.

After all the data has been downconverted, phase and time aligned, averaged over the number of PN sequence periods, and downsampled by a factor of 10, it is ready to be processed by the iterative MLE algorithm. The algorithm begins by column stacking the received data matrix, where each column represents the signal received on each antenna. The calibration matrices, U_m, for $m = 1, \ldots, 60$ are likewise column stacked. The signal

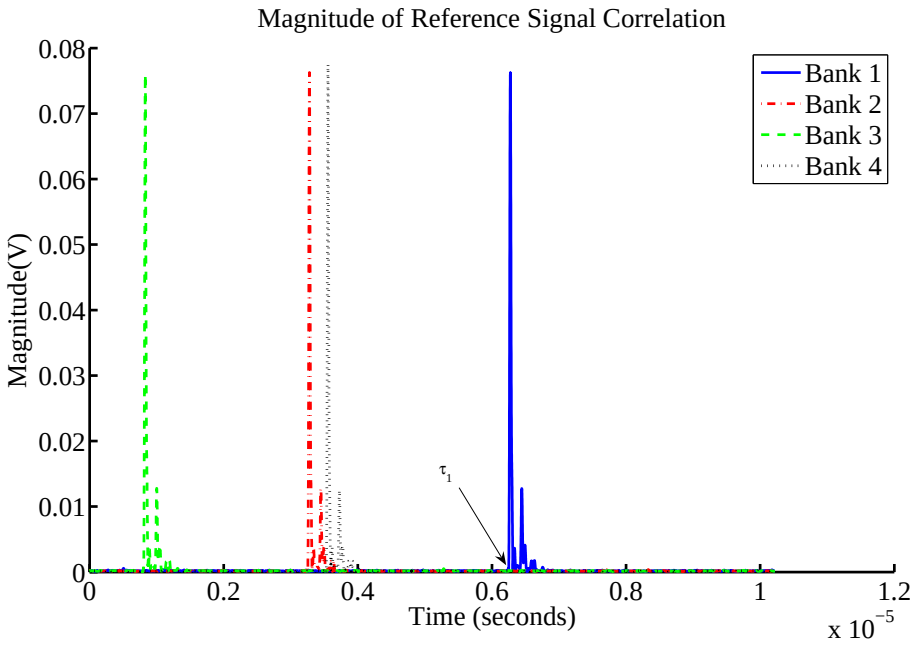

Fig. 3.16: Time alignment of reference signals using correlation with PN code.

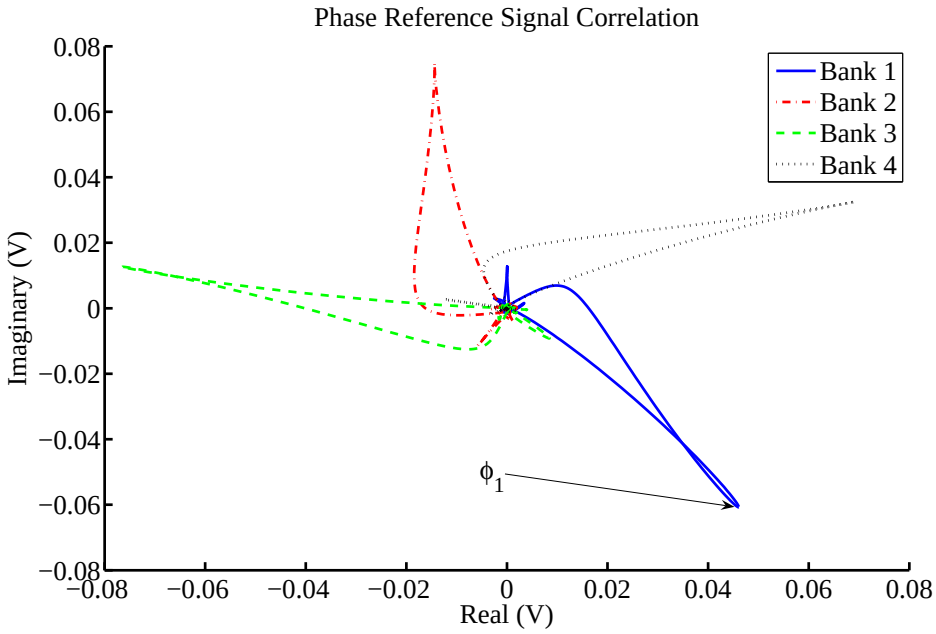

Fig. 3.17: Phase alignment of reference signals using correlation with PN code.

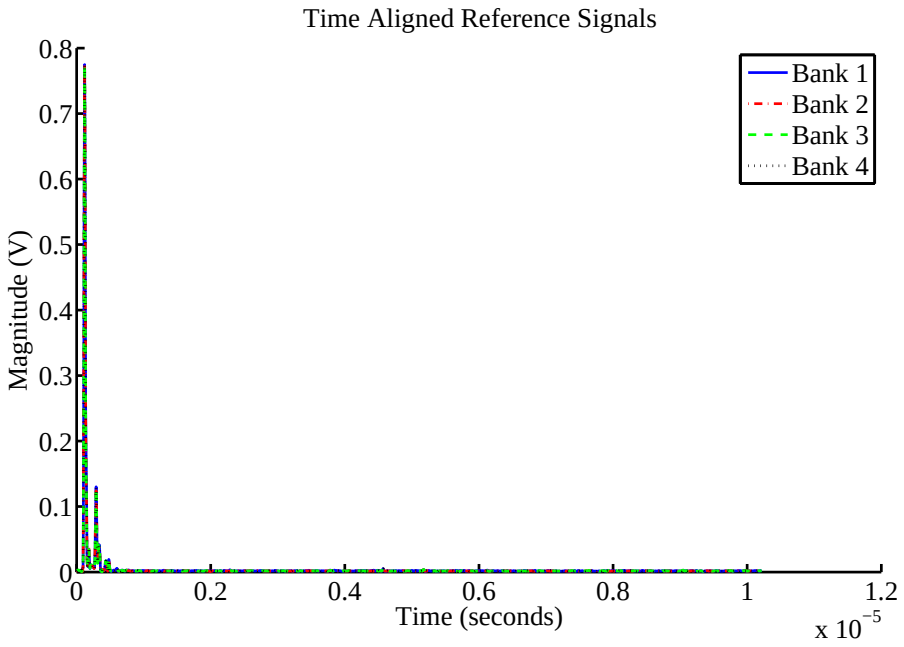

Fig. 3.18: Time aligned reference signals.

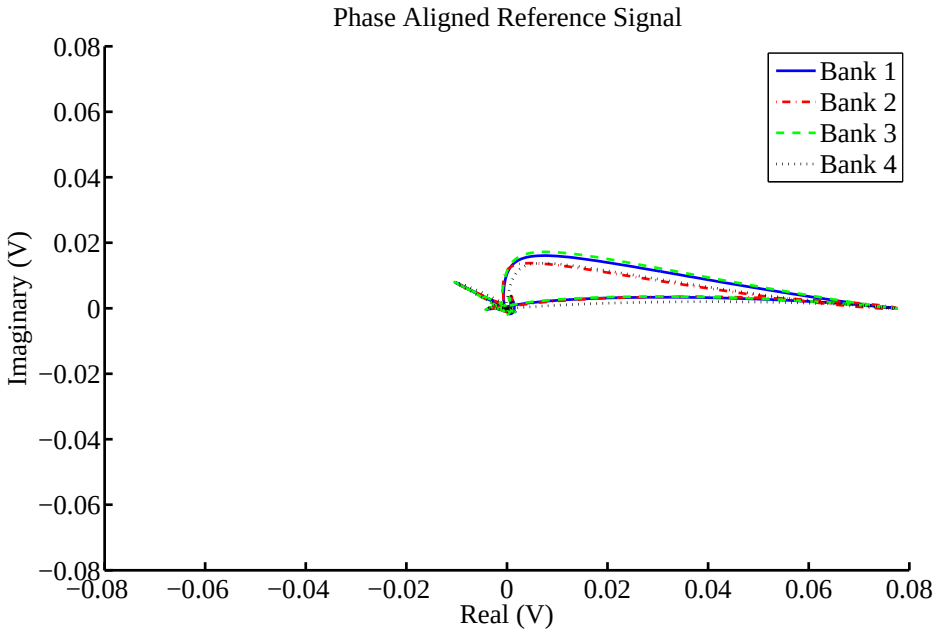

Fig. 3.19: Phase aligned reference signals.

model of eq. (2.11) in the noiseless case becomes

$$\mathbf{v} = \sum_{\mathbf{l=1}}^{\mathbf{L}} \mathbf{u_l} \alpha_\mathbf{l} \tag{3.7}$$

where the boldface $\mathbf{v}$ and $\mathbf{u}$ represent the column stacked versions of the recieved signal and calibration matrices, respectively. Equation (3.7) can be rewritten in matrix form as

$$\mathbf{v} = U\alpha = \left[\begin{array}{c} \\ \mathbf{u_1} \cdots \mathbf{u_L} \\ \\ \end{array} \right] \left[\begin{array}{c} \alpha_1 \\ \vdots \\ \alpha_L \end{array} \right] \tag{3.8}$$

where α is now an $(L \times 1)$ vector of complex signal amplitudes. Furthermore,

$$\alpha = U^{+}\mathbf{v} \tag{3.9}$$

where $(\cdot)^{+}$ denotes matrix pseudo-inverse. The cost function in eq. (2.16) needs to be minimized and can be expressed as

$$arg \min_{\alpha} \|\mathbf{v} - U\alpha\|_F^2. \tag{3.10}$$

By substituting eq. (3.9) into eq. (3.10) leads to

$$arg \min_{n_l, \phi_l} \|(I - UU^{+})\mathbf{v}\|_F^2. \tag{3.11}$$

A graphical representation of eq. (3.11) is given in fig. 3.20. As discussed in Chapter 2, each time-shifted version of each calibration matrix forms a basis function, U_{mn}. The projection of the received signal vector, $\mathbf{v}$, onto each basis function is maximized by either minimizing the vector $\mathbf{y}$, or maximizing the vector $\mathbf{x}$. The length of $\mathbf{y}$ is equivalent to the squared Frobenius norm of eq. (3.11). To minimize $\mathbf{y}$ it would be necessary to create an indentity matrix that is $(KN \times KN)$, which for K=12 antennas, and N=2555 times samples is (30660×30660) and is far too much memory for desktop personal computers to allocate.

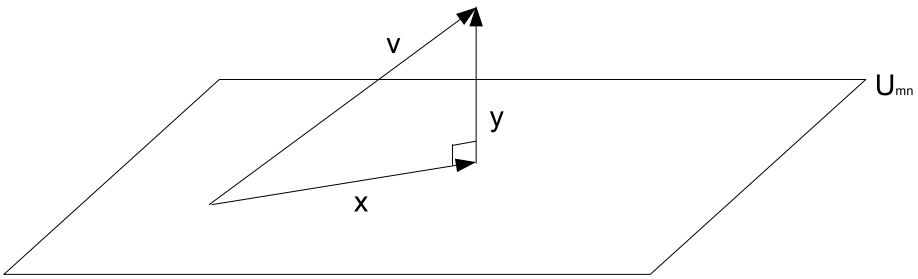

Fig. 3.20: Signal subspace created by calibration basis functions.

On the other hand, maximizing $\mathbf{x}$ is done by maximizing the following cost function

$$arg \max_{n_l, \phi_l} \|UU^{+}\mathbf{v}\|_F^2 \tag{3.12}$$

that can be simplified to

$$arg \max_{n_l, \phi_l} (U^H \mathbf{v})^H (U^H U)^{-1} (U^H \mathbf{v}). \tag{3.13}$$

In order to iteratively solve for all L values of $\hat{\theta}^L$, eq. (3.13) is first evaluated for each $U^1 = [\mathbf{u}_i]$ for $i = 1, \ldots, M \times N$ where the superscript denotes the iteration number and model order. The matrix ,U^1, that maximizes eq. (3.13) and the corresponding index, i^1, are retained for use in each successive iteration. The complex amplitude, α^1, is found using eq. (3.9). For the l^{th} iteration eq. (3.13) is evaluated for each $U^l = [U^{l-1}\mathbf{u}_i]$ for $i \neq i^{l-1}, \ldots i^1$.

Chapter 4

MLE Simulations

Several simulation cases were developed to verify the performance of the iterative MLE algorithm. Since the received signal is a summation of the fields of all the multipath signal components, a received signal matrix, V, can be simulated by summing scaled and time-shifted versions of the calibration matrices corresponding to the simulated TOAs and AOAs. Complex white Gaussian signal noise was then added to the total received signal. The simulations were performed to verify the accuracy of the method and to determine the spatial and temporal resolution.

4.1 Noiseless Simulations

The first type of simulations studied were noiseless to verify that the algorithm functions properly. The angular and temporal resolution are verified to be equal to 6 degrees in azimuth, and 4 ns, which are respectively the spatial and temporal sampling periods of the calibration measurements.

4.1.1 Angular Resolution

To determine the angular resolution of the algorithm, simulations were performed for two signals that arrive at the same time, but with different AOAs. Angular separations of 6, 30, 42, and 90 degrees were simulated. The values of the first order cost function, eq. (3.13), for a signal arriving at a time delay of zero, and AOA of zero are plotted in fig. 4.1. Because of a finite number of antenna elements and signal bandwidth, the peak of the cost function is spread in both the angular and temporal domains. The angular width of the peak is about 60 degrees while the temporal width is about 40 ns. If two signals arriving at the same time are separated by more than about 40 degrees, two peaks will be

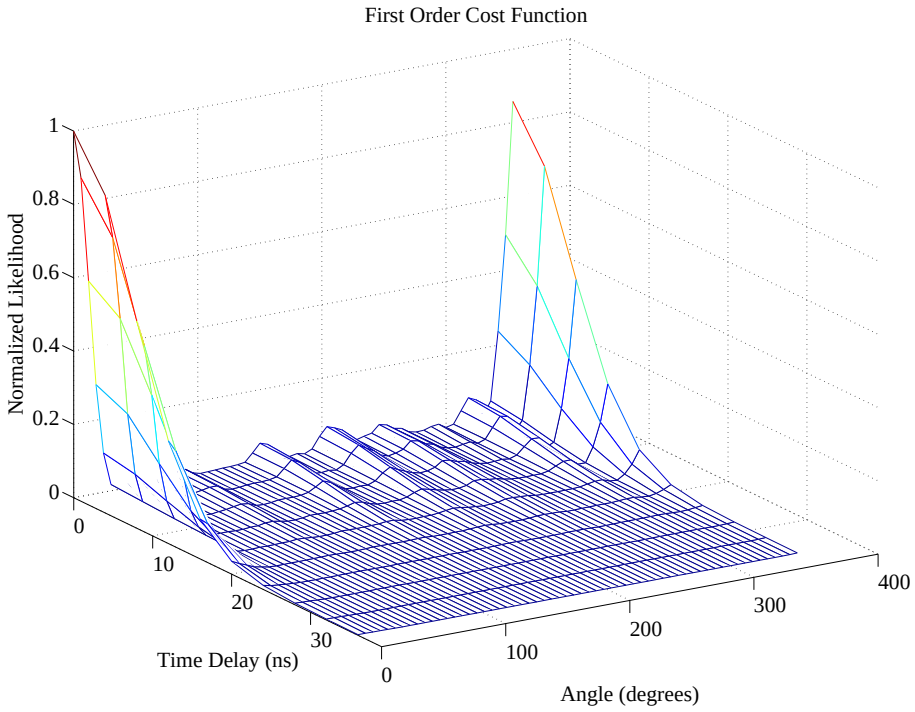

Fig. 4.1: First order cost function for a single arrival at zero degrees.

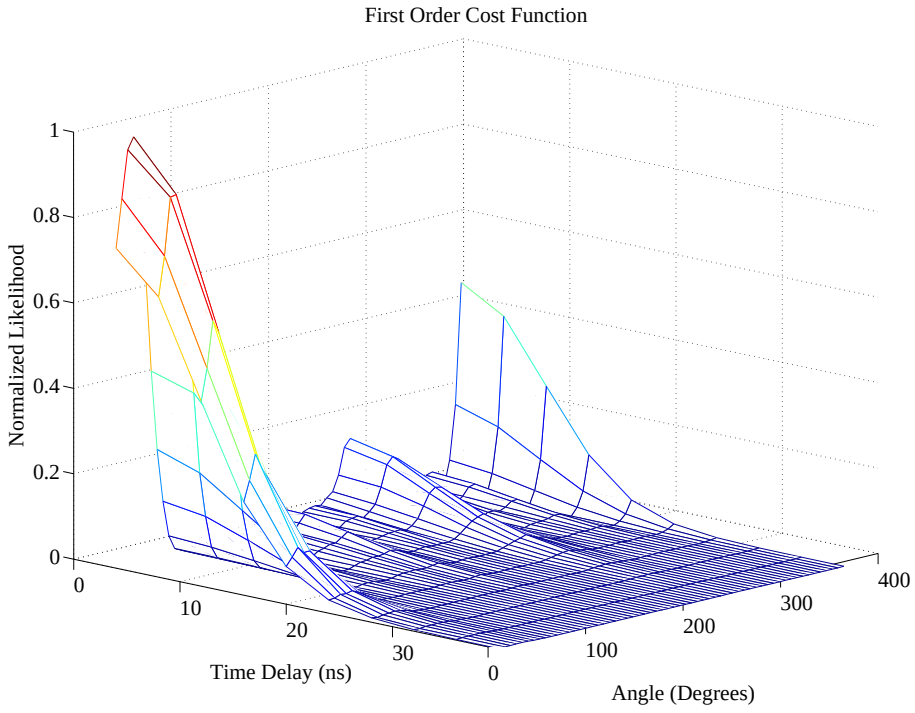

Fig. 4.2: First order cost function for AOAs of 0 degrees and 30 degrees.

Table 4.1: Iterative parameter estimation for AOAs of 0 and 30 degrees.

Iteration	Angle (degrees)	Time (ns)	Normalized Magnitude	Energy (%)
1	18	0	1.34	77.8
2	18 354	0 0	1.17 0.55	90.9
3	18 354 30	0 0 0	0.54 0.75 0.75	97.8
4	18 354 30 0	0 0 0 0	0.00 0.00 1.00 1.00	100

present in the cost function at the correct angles and time delays. The stronger signal will be selected at the first iteration and the weaker signal at the second iteration. However, if the angular separation is less than about 40 degrees, the two peaks merge into one, and the number of iterations needed to find the true (unbiased) estimates is greater than the number of signal arrivals. For an example of a case where the cost function peaks merge into one, two signals arriving at a time of 0 ns and separated by 30 degrees were simulated. The cost function is given in fig. 4.2. At the first iteration an AOA of 18 degrees is estimated. Since the estimated arrival at 18 degrees will not account for all of the signal energy, as the model order is increased, the unbiased values will eventually be estimated. When all the unbiased values have been estimated the values of alpha for the incorrect estimates are zero. The parameters estimated at each iteration are given in table 4.1. For each simulation with separations of 6, 30, 42, and 90 degrees the unbiased parameter estimates were found by the fourth iteration.

4.1.2 Temporal Resolution

To determine the algorithm's temporal resolution, two signals were simulated to arrive at the same angle, but separated in time by 4, 12, and 30 ns, where 4 ns is the time between samples. The first order cost function for the case where both signals arrived at 180 degrees and separated by 12 ns is shown in fig. 4.3. Table 4.2 gives the parameter estimates at each iteration. In each case the algorithm found the unbiased estimates by the fourth iteration.

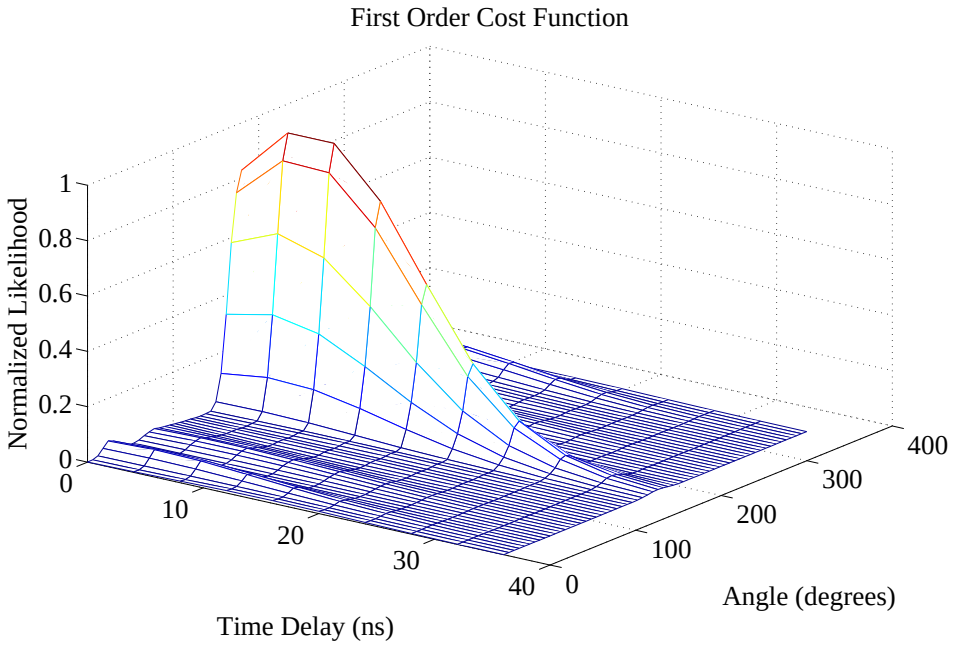

Fig. 4.3: Cost function for two signals separated by 12 ns.

Table 4.2: Iterative parameter estimation for TOAs 0 and 12 ns.

Iteration	Angle (degrees)	Time (ns)	Normalized Magnitude	Energy (%)
1	180	4	1.67	92.0
2	180 180	4 16	1.40 0.53	98.6
3	180 180 180	4 16 0	0.89 0.63 0.51	99.4
4	180 180 180 180	4 16 0 12	0.00 0.00 1.00 1.00	100

4.1.3 Conclusions for Simulations without Noise

In both noiseless simulation cases the algorithm's resolution was only limited by the spatial and temporal sampling rates. If either the signal sampling rate or the number of calibration measurements were increased, the resolution of the algorithm would also increase accordingly. If all of the multipath signals are separated by about 20 ns or 30 degrees in azimuth, the algorithm will estimate each signal successively in order of decreasing power. However, if the signals are not sufficiently separated in angle or time, the algorithm will require more iterations than the number of signals to be estimated. This fact complicates the task of determining how many iterations are needed to estimate the unbiased signal parameters. A method for estimating the number of required iterations has not yet been determined. A sufficient method would be to iterate more times than needed. For large SNR's the method works well, but if the SNR is not high enough, the signal amplitude estimates will deviate from their unbiased estimates.

4.2 Direction of Arrival Simulations with Noise

Noiseless simulations were done to verify that the algorithm functions as formulated and to verify the super-resolution capabilities of the algorithm in the ideal case. Like all algorithms, the accuracy and resolution of the MLE are expected to decrease with decreasing SNR. However, the Cramer-Rao lower bound (CRLB) on the variance of the error of the estimates can be approached as the number of snapshots increases [20]. In other words, the MLE algorithm is an efficient estimator, which is defined as an unbiased estimator that acheives the CRLB [20].

A simulation case was developed to determine the effect of noise on a measurement consisting of a cluster of three closely spaced signal arrivals and another signal whose power is 20 dB weaker than the strongest component. Table 4.3 shows the signal parameters involved. Simulations were run for SNR's of 30, 20, 10, 0, and -10 dB. For each case where the SNR was above 0 dB, the unbiased parameters were estimated on the 8^{th} iteration. Figure 4.4 shows a plot of the unbiased parameter estimates, while fig. 4.5 shows the estimates at the 5^{th} iteration and is included to show the effect of too few iterations. After five iterations,

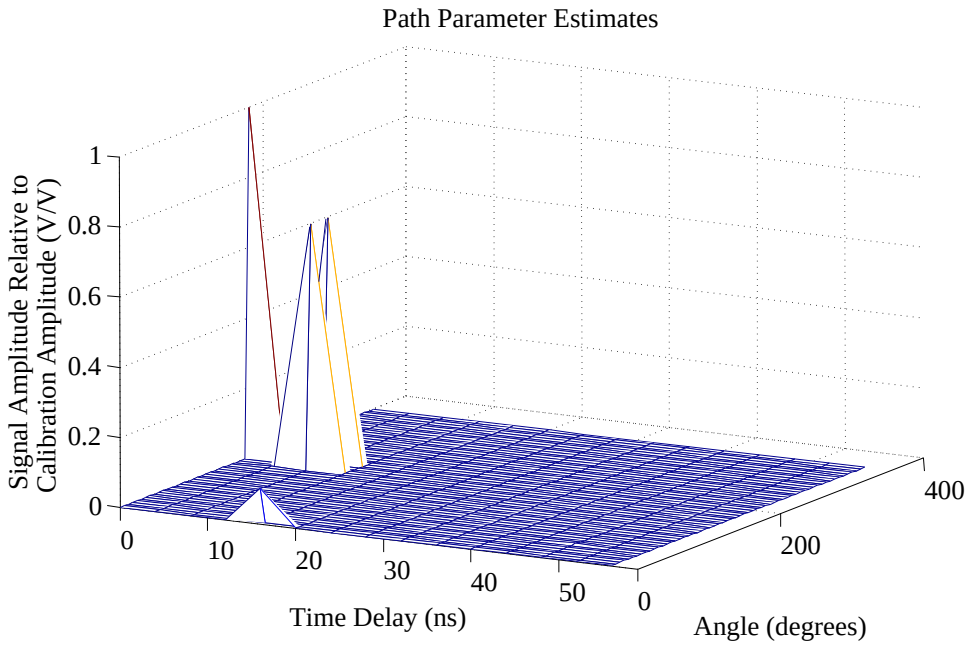

Fig. 4.4: Multipath parameter estimates for an SNR of 30 dB after 8 iterations.

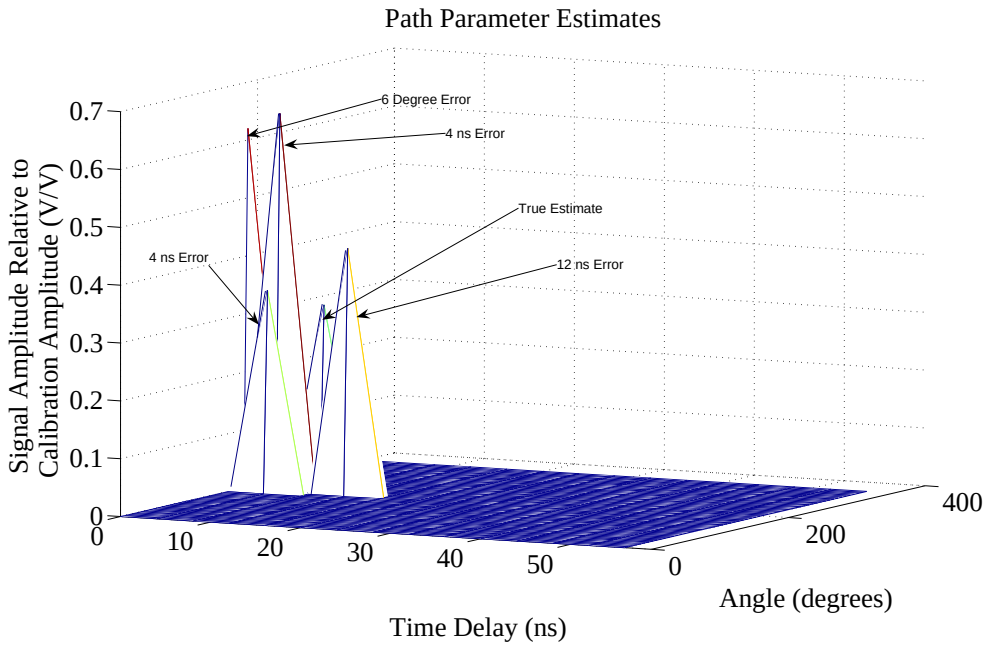

Fig. 4.5: Multipath parameter estimates for an SNR of 30 dB after 5 iterations.

Table 4.3: Signal parameters for the noisy simulations.

Angle (degrees)	Time (ns)	Normalized Magnitude
180	0	1.0
172	8	0.7
188	8	0.7
0	16	0.1

only one of the unbiased estimates has been found as noted in fig. 4.5. The algorithm finds a cluster of signal energy arriving near 180 degrees between 0 and 12 ns. Super-resolution is finally acheived after a sufficient number of iterations have been performed.

For the 0 dB SNR case, ten simulations were repeated. Six of the simulations returned the unbiased parameter estimates. For the other four cases, super-resolution was not achieved. Figure 4.6 shows how the signal estimates can be spread in time and angle when the SNR is too low. A higher SNR can be achieved if multiple measurement snapshots are averaged prior to estimating the multipath parameters. By averaging five snapshots with an SNR of 0 dB each, the unbiased parameters were estimated 10 out of 10 trial simulations. Furthermore, the benefits of averaging are shown in fig. 4.7 and fig. 4.8. Figure 4.7 contains the parameter estimates when an SNR of -10 dB was simulated. The main cluster of signals arrive near the true parameters, but spread in time and angle. For this particular simulation, noise estimates were found at 8, 26, and 40 ns, as indicated by the arrow. The signal arriving at 0 degrees and a delay of 16 ns is estimated at 354 degrees and a delay of 16 ns, an error of six degrees. Figure 4.8 shows the estimates when 20 snapshots were averaged prior to parameter estimation. The unbiased parameters are estimated correctly. The noise estimates, indicated in the figure, are highly attenuated compared to the results without averaging.

4.3 Algorithm Efficiency

The simulations showed that if the received signal matrix is constructed from the calibration matrices and the signal to noise ratio is greater than 0 dB, the correct angle and time estimates will be found. The accuracy of the estimated signal magnitude will increase with increasing SNR. For measurements with an SNR less than 0 dB, the correct

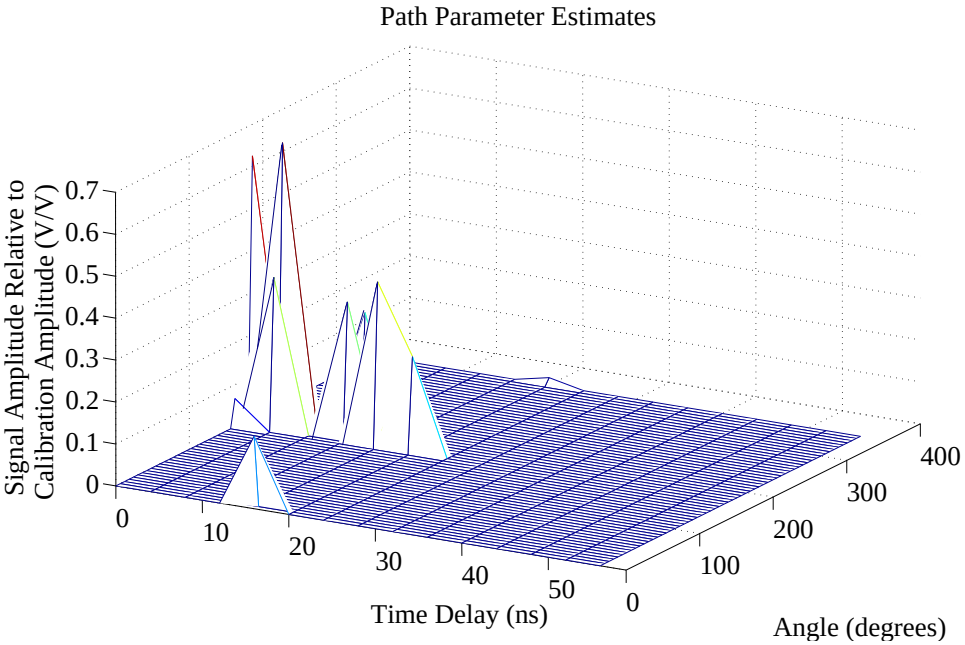

Fig. 4.6: Multipath parameter estimates for an SNR of 0 dB.

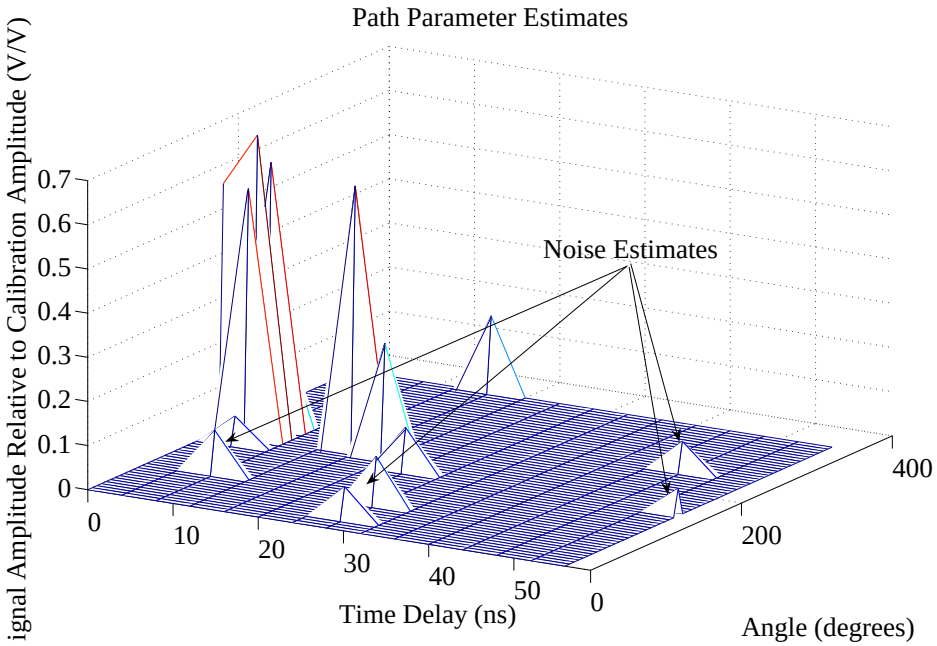

Fig. 4.7: Multipath parameter estimates for an SNR of -10 dB.

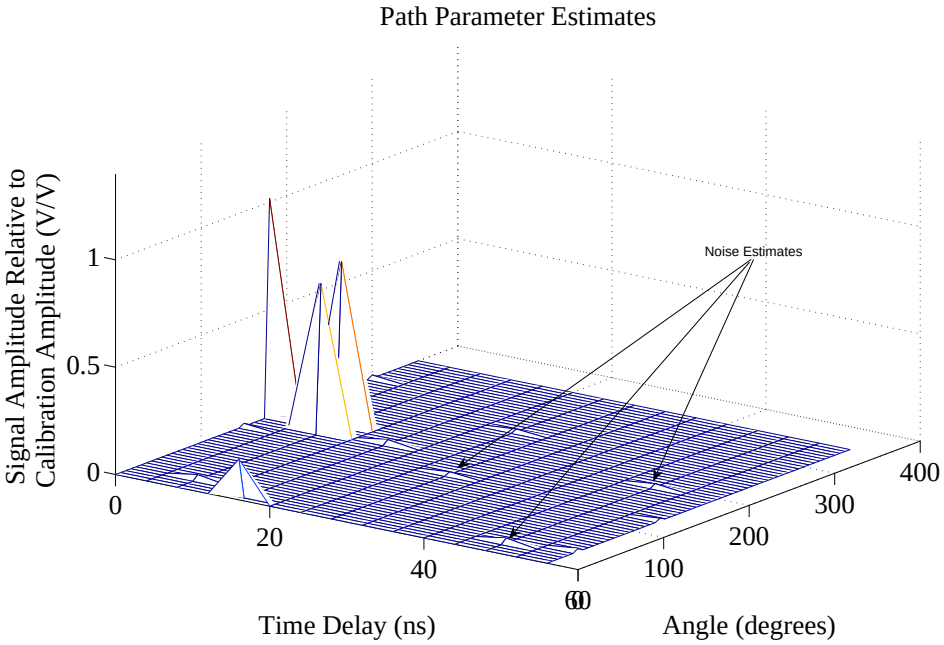

Fig. 4.8: Average of 20 snapshots with an SNR of -10 dB.

estimates may still be found if enough snapshots are averaged together. If L signals are sufficiently spaced in the angular and temporal domains so that their cost function peaks do not overlap, the algorithm correctly estimates the multipath parameters in L iterations. If the number of iterations is greater than L, the algorithm begins to estimate noise. If the signals are not spaced sufficiently, the average time and angle are detected. Eventually the true parameters will be estimated, but more than L iterations are required to find L signals. A method to determine when the true parameters have been detected in a noisy environment has not yet been determined.

Because the algorithm will, with enough samples, approach the CRLB, a comparison with the MLE algorithm is often made when determining the efficiency of other signal processing algorithms [21]. The MLE was used in this experiment because it includes the calibration as a function of AOA in the signal model and gives as good or better results than other algorithms. However, due to the multidimensional search of all angles and delays, it is the most computationally complex of the widely used algorithms. Equation (4.1) shows the size of the complex matrix multiplications required to calculate a single value of the

cost function of eq. (3.13) where l is the iteration number, and 30660 comes from column stacking 12 columns of 2555 samples each. A total of $M \times N - l$ cost function values are calculated during the l^{th} iteration where $M = 60$ is the number of discrete angles searched, and N is the number of discrete time delays searched. The value of N is determined for each measurement by inspecting the correlation of the received signal with a copy of the transmitted PN code and noting the time delay of the last significant signal echo. For indoor measurements and a sampling rate of 250 MHz, the value of N ranges from about 80 to about 180, corresponding to time delays of 320 and 720 ns, respectively. The amount of time required for a single iteration greatly increases as the iteration number increases. A desktop personal computer required less than a minute of processing time to estimate one signal for $M = 60$ angles and $N = 150$ timed delays, and more than 10 hours to estimate a total of 60 signals with the same parameters.

$$[(l \times 30660) \times (30660 \times 1)]^H [(l \times 30660)(30660 \times l)]^{-1} [(l \times 30660)(30660 \times 1)] \quad (4.1)$$

The processing time required to accurately estimate all of the dominant multipath components in a non-line-of-sight measurement requires modifications in order to be practical in terms of required processing time. In order to decrease the processing time, either fewer time samples or angular samples must be used. Using 30 of the 60 calibration matrices will cut the processing time in half, but will decrease the angular resolution by a factor of 2. On the other hand, signal downsampling will improve the processing time with a decrease in the temporal resolution. Another option would be to use a shorter length PN code, which would decrease the processing gain and therefore the effective SNR. Using a 511 bit code for low SNR measurements and a shorter code for high SNR measurements would require a full array calibration to be performed for each PN code length, but would allow for faster measurements when sufficient SNR is attainable. A further decrease in SNR would result if the received data and calibration matrices are truncated in time, so that the first N samples only are used in the algorithm. However, simulations showed that if enough snapshots were used to increase the SNR, the algorithm still returned the unbiased parameter when using

the first 15 bits of a 511 bit PN sequence, thus reducing the computational load by a factor of 16.

Chapter 5

Measurement Results

Measurements were carried out to verify the performance of the channel sounder and multipath signal processing algorithm, and to attempt to trace the dominant signal paths from the transmitter to the receiver, thereby correlating the measured data with the expected channel response based on a specific physical environment. Initially, a small set of measurements were made on the same field where the calibration measurements were made in an attempt to verify the accuracy and repeatability of the calibration measurements. The remaining measurements were made inside the four buildings of the engineering complex on campus. Indoor measurements consisted of the following types: LOS hallway propagation, hallway diffraction, NLOS hallway, classroom to hallway, classroom to classroom. Since one channel snapshot requires 21 seconds, all measurements were made during the night to minimize the time varying effects of the channel on the measurements.

5.1 Calibration Test Measurements

To test the accuracy of the calibration measurements, the transmitter and receiver were taken to the location of the calibration measurements about one month after the original calibration was performed. The calibration measurement for an AOA of zero degrees was repeated. Figure 5.1 and fig. 5.2 show the path parameter estimates after one iteration and 20 iterations, respectively. After a single iteration, the LOS component is estimated at 0 degrees and at a delay of 40 ns, corresponding to a 12 meter propagation path. Further iterations estimate a dominant cluster of signals between 352 degrees and 6 degrees, as noted in fig. 5.2, and multiple weaker signal arrivals within 16 ns of the LOS component, scattered throughout various angles. The measurement system inaccuracy is evidenced by the false signal estimates since the observed scattering effect cannot be caused by signal reflections.

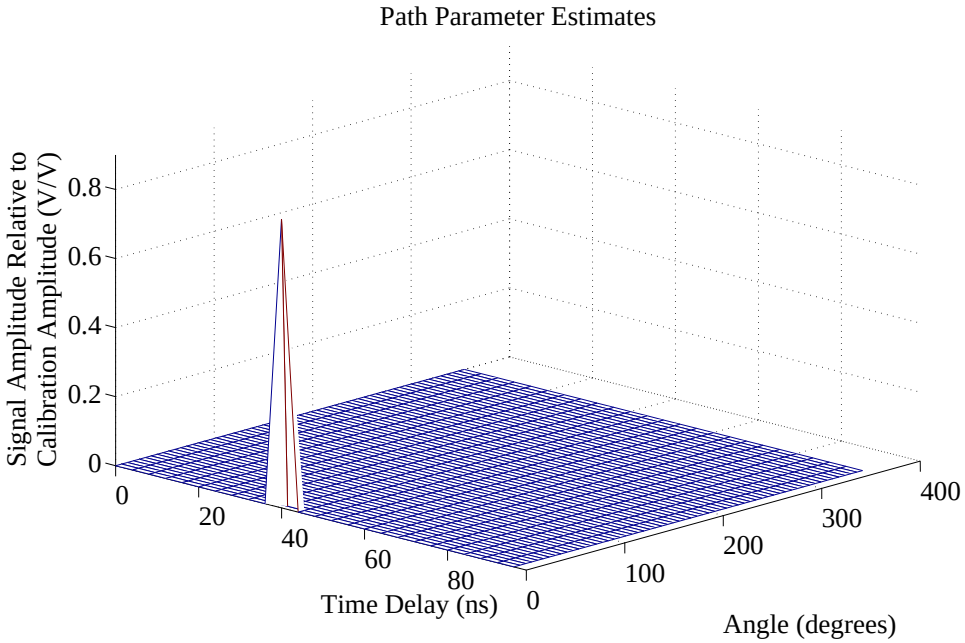

Fig. 5.1: Parameter estimates for calibration test measurement after 1 iteration.

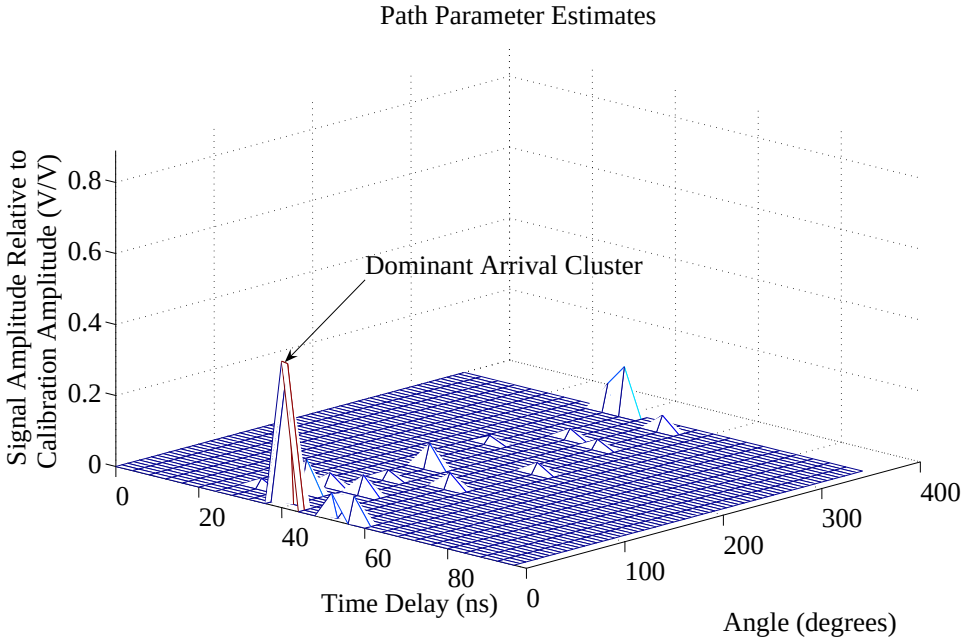

Fig. 5.2: Parameter estimates for calibration test measurement after 20 iterations.

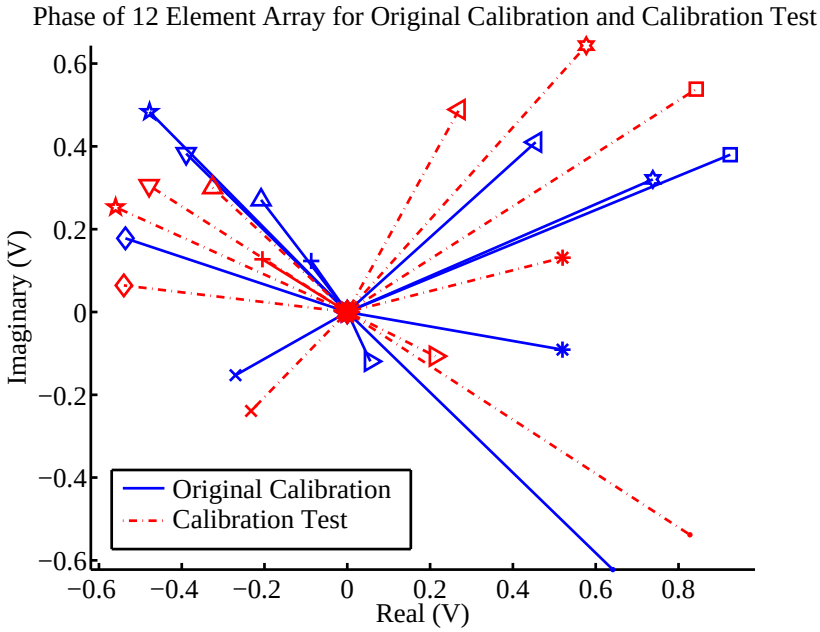

Fig. 5.3: Phase comparison for outdoor measurement.

One possibile cause of the false estimates is receiver noise. However, simulations showed that if the SNR was greater than 0 dB, false estimates based on noise were negligible. More likely causes of the false estimates are small changes in antenna position, phase drift in the RF circuitry, the false assumption that the channel is completely stationary during the measurement time, and bias introduced due to the fact that the calibration matrices are not orthogonal. Figure 5.3 compares the phase of each element of the array for the original zero degree calibration matrix and for the test measurement. Each symbol represents a different antenna of the array. Because the calibration measurements have shifted, the signal processing algorithm is expected to return some false estimates. To minimize false estimates a more accurate calibration is required.

5.2 Calibration Improvements

After the majority of the measurements were made it was discovered that two antennas were displaced by about one centimeter from their original calibrated positions. Since all equipment was originally hand tightened, this displacement likely occurred while transport-

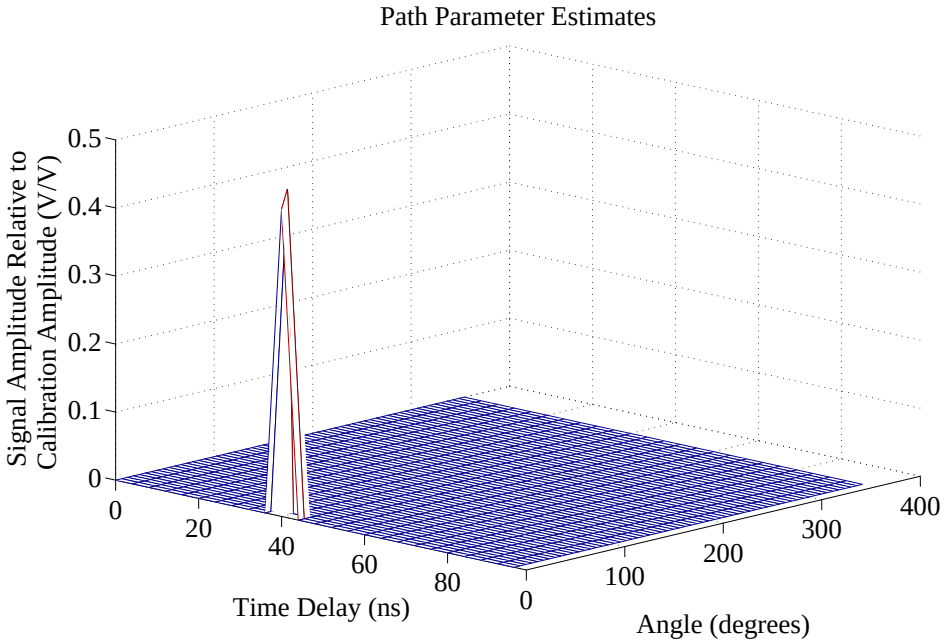

Fig. 5.4: Parameter estimates for an AOA of 3 degrees after 2 iterations.

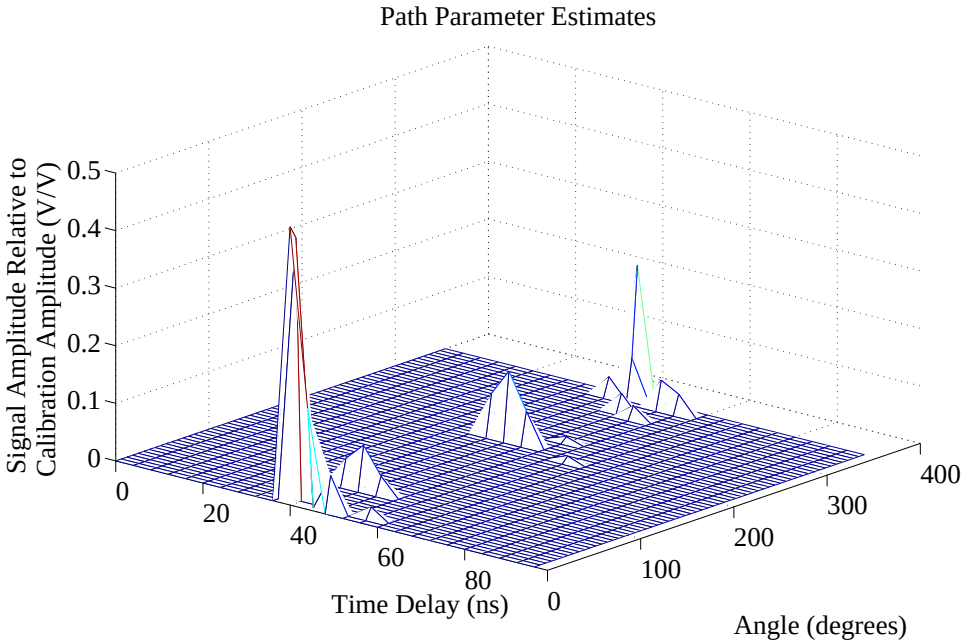

Fig. 5.5: Parameter estimates for an AOA of 3 degrees after 20 iterations.

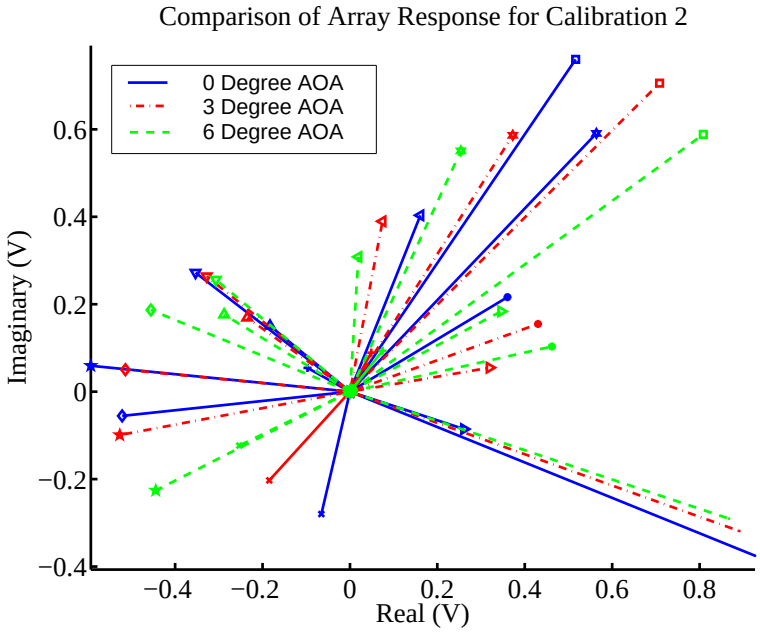

Fig. 5.6: Phase comparison for repeat calibration.

ing the measurement equipment to and from the calibration location across sidewalks with large cracks. Due to the noted array changes, the receiver was rebuilt with all antennas and RF hardware firmly mounted in place. Furthermore, all RF cables were straightened and arranged to avoid any changes in the layout and bending of the cables. After the receiver was rebuilt, a second calibration was performed in the same manner and location as the first. The number of snapshots per discrete AOA was increased from 9 to 57 in an attempt to increase SNR by averaging over more PN sequence periods.

The calibration measurements were made from 10:00 p.m. until 2:00 a.m. on a breezy night. There was no noticeable movement in the receiver antennas, but the parabolic transmit antenna was often displaced up to a few centemeters by the wind. This could lead to some inaccuracy but the exact effect of it is unclear. After all 60 discrete AOA measurements were made, an AOA of 3 degrees was measured to determine the accuracy when a signal arrives at an angle that has not been calibrated. Figure 5.4 shows that after two iterations, two signals are estimated at 0 degrees and 6 degrees as expected. Figure 5.5 shows the results after 20 iterations. Since the measurement was made immmediately after

the 6 degree AOA calibration measurement, the resulting false estimates are most likely due to bias from non-orthogonal basis functions or changes in the environment during the snapshot and calibration measurement times. Figure 5.6 shows the changes in phase for the 0 degree, 3 degree, and 6 degree measurements. Since the lines representing the phase on the 12 elements for the 3 degree measurement are consistently between the other two, it can be assumed that the phase drift of the RF circuitry is negligible over the calibration period of four hours.

5.3 LOS Measurements Along a Hallway

Indoor LOS hallway measurements were perfomed on the second floor of the Engineering Lab (EL) building with different transmitter to receiver separations. The Appendix gives detailed transmitter and receiver locations relative to the local surroundings, along with a picture of the hallway. Figure 5.7 (created according to research by Jared Bench) shows the relative positions of the transmitter and receiver. In each measurement case the transmitter remained in the position shown. The receiver orientation is shown by a red arrow marking the direction of 0 degrees. Angles are measured counterclockwise from the 0 degree reference. For each measurement position the receiver was oriented with zero degrees facing the transmitter. Ten measurements were made along the length of the hallway. All doors were closed to the classrooms on both sides of the hallway. The only objects protruding from the flat walls are a drinking fountain, a clock, and a fire-extinguisher, all located within a meter of each other.

The estimated path parameters for the receiver position marked RX1 in fig. 5.7 are shown in fig. 5.8. The multipath parameters for each marked peak are given in table 5.1, while fig. 5.9 shows the path of the signals corresponding to each marked peak. A LOS signal, a reflection from the wall behind the transmitter, a reflection from the wall behind the receiver, and a reflection from a fire extinguisher are all detected. Two more signals that arrive at the same time as the LOS signal are detected at 30 degrees and 330 degrees. Although the expected AOAs of a single reflection from the wall are 17 degrees and 343 degrees, the estimated reflections are symmetric and could be an average of multiple reflec-

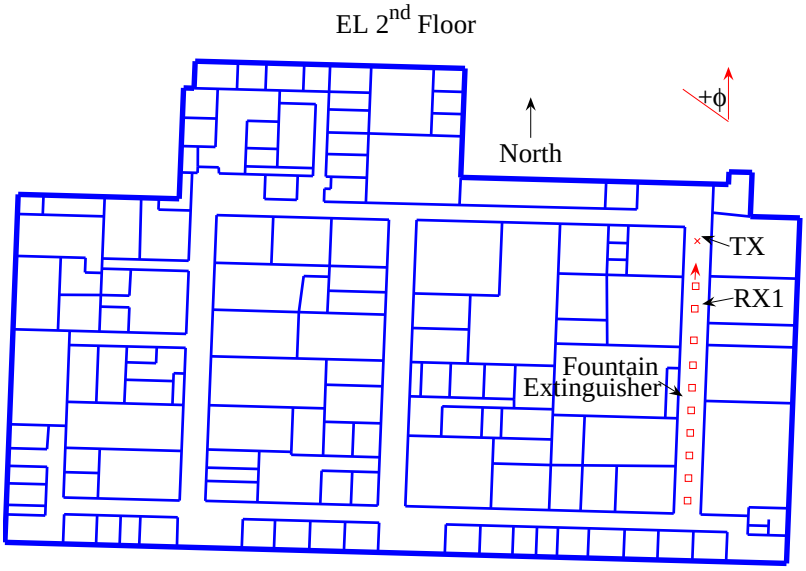

Fig. 5.7: Locations of transmitter and receiver for LOS hallway measurements.

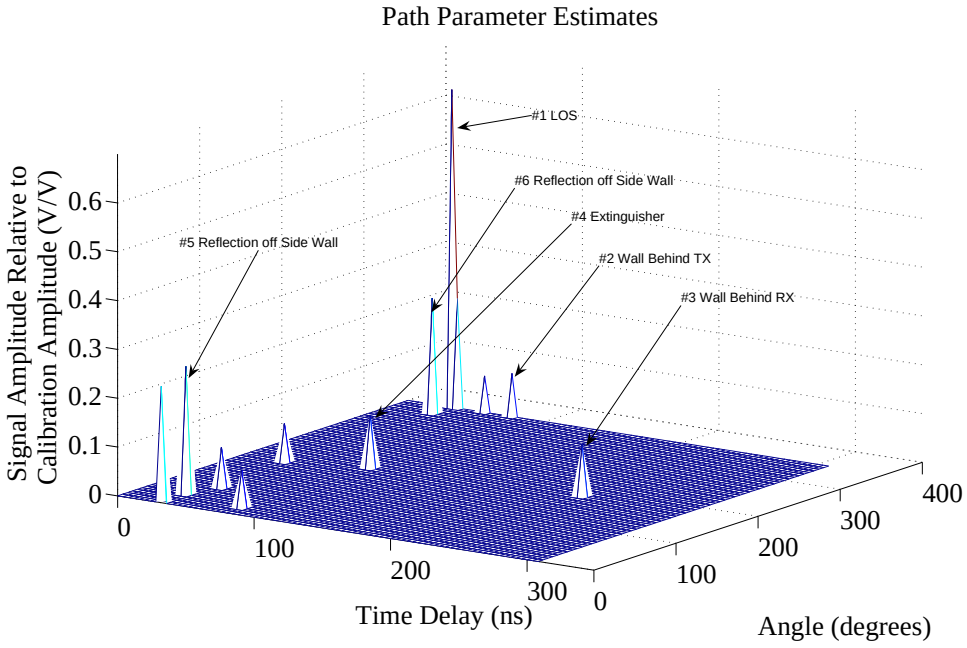

Fig. 5.8: Hallway signal parameter estimates for position RX1.

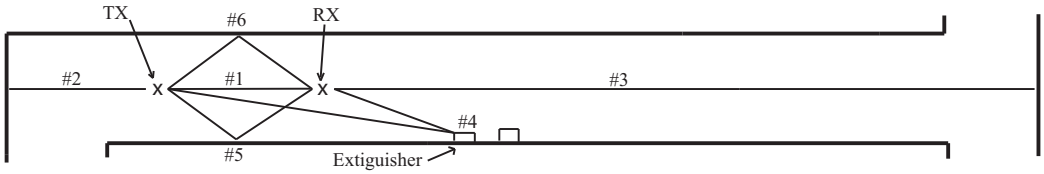

Fig. 5.9: Parameter estimates correlated with actual paths.

Table 5.1: Parameter estimates for receiver location RX1.

Path #	Path Length (m)	Expected AOA (degrees)	Estimated AOA (degrees)	Expected TOA (ns)	Estimated TOA (ns)
1	9.1	0	354	30.3	32
2	23.7	0	354	79.0	76
3	68.7	180	180	229.0	232
4	25.5	171	168	85	84
5	9.7	17	30	32.2	32
6	9.7	343	330	32.2	32

tions from the walls. Each of the first four paths listed in table 5.1 correspond with the expected values to within 6 degrees and 4 ns.

Similar results were found for each of the other nine receiver positions. In each case a LOS signal, a reflection from the wall behind the transmitter, and a reflection from the wall behind the receiver were estimated correctly to within the system resolution. The fire extiguisher was only detected for the positions where the extinguisher and transmitter were on opposite sides of the receiver. When they were both on the same side of the receiver, both signals were near 0 degrees and any reflection from the extiguisher or fountain was unresolveable.

5.4 NLOS Measurements Along a Hallway

Measurements were made on the 4^{th} floor of the Engineering Building (ENGR) at the locations show in fig. 5.10 (created according to research by Jared Bench). The Appendix gives precise locations and pictures of the measurement environment. Two key differences between the hallways in ENGR and EL are the building support beams that protrude about 10 cm from the walls in ENGR, and the many classrooms and offices, in ENGR, that are recessed from the main hallway creating small “coves.” Signal diffraction will occur both

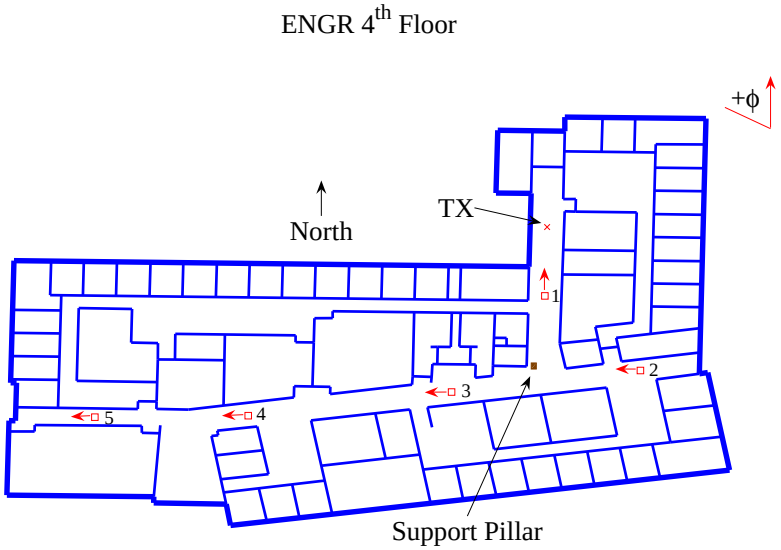

Fig. 5.10: Locations of 4^{th} floor diffraction measurements.

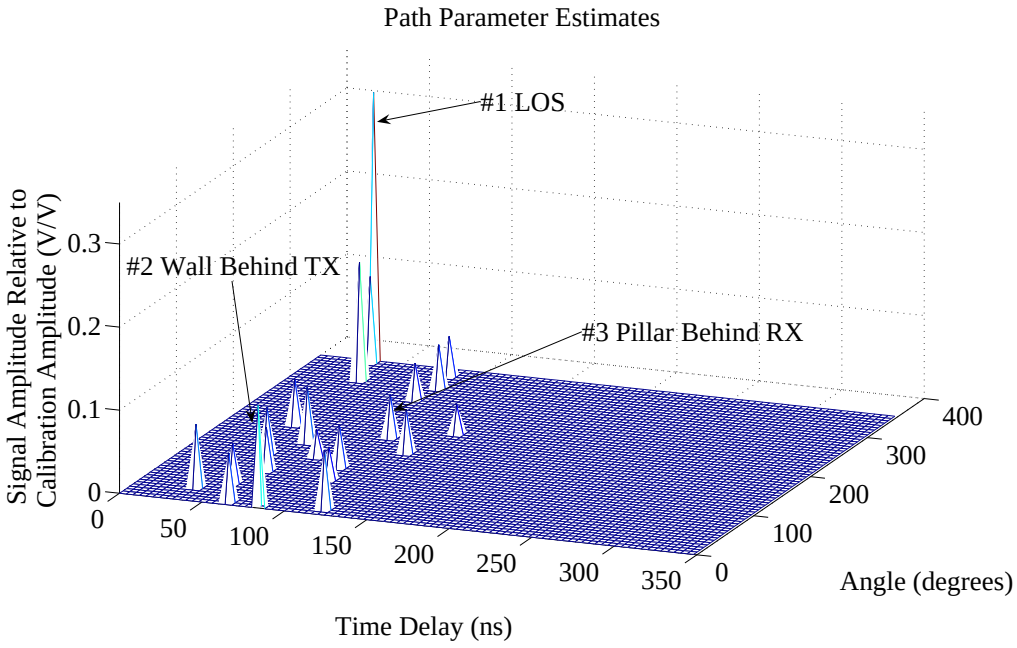

Fig. 5.11: 4^{th} floor LOS measurement 1.

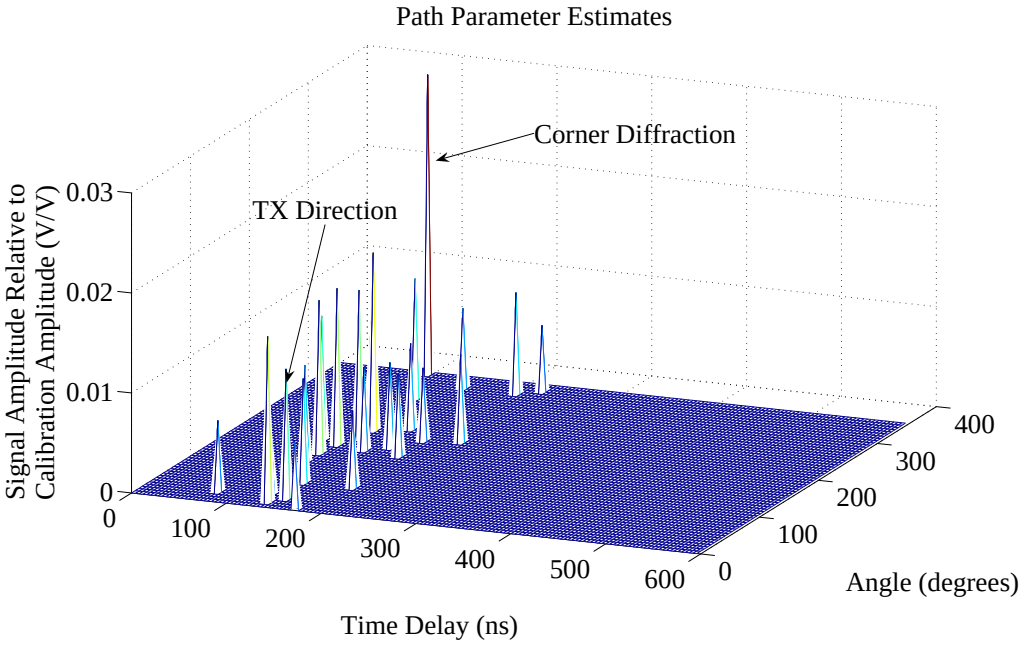

Fig. 5.12: 4^{th} floor NLOS measurement 2.

at the corners of the beams and the "coves." The measurements were made to compare LOS hallway measurements with NLOS diffraction measurements. For the LOS case, shown in fig. 5.11, the receiver was oriented with zero degrees facing the transmitter. Table 5.2 gives the parameters of the peaks that correspond well to the expected signal arrivals. As expected the largest signal component arrives from the LOS direction, but with an error of 6 degrees. The signal reflected from the wall behind the transmitter arrives at the 0 degrees and and at 84 ns, both within the system resolution of the expected values. The third signal, labeled in fig. 5.11 as "Pillar Behind TX," is estimated to arrive at 156 degrees at 100 ns. The true arrival would be at about 175 degrees and at 94.3 ns. Although these values are not exact, the time delay corresponds well enough to be a reflection from the pillar. Error in the angular value can easily be attributed to imperfections in calibration and a non-static environment.

For measurement positions 2-5 the receiver was oriented with zero degrees facing west. Figure 5.12 shows the parameter estimates from receiver position 2, which is located seven meters east of the LOS hallway. The strongest signal component shown arrives at the

Table 5.2: Parameter estimates for receiver location 1 in ENGR.

Path #	Path Length (m)	Expected AOA (degrees)	Estimated AOA (degrees)	Expected TOA (ns)	Estimated TOA (ns)
1	10.1	0	354	33.7	32
2	25.9	0	0	86.3	84
3	28.3	175	156	94.3	100

receiver at 354 degrees. A signal that was diffracted from the corner of the transmitter hallway would arrive at the receiver from an angle of 357 degrees, hence it is assumed that the strongest path is indeed a signal diffracted from the corner of the transmitter hallway. The estimated signals in fig. 5.12 are divided into two distinct clusters. The signal power appears to arrive clustered around 0 and 180 degrees. Many signal echoes appear, and are likely due to reflections from the support beams and diffractions from the "cove" corners. Figure 5.13 shows the results from receiver position 3 which was located seven meters west of the transmitter hallway. Like the results from receiver position 2, fig. 5.13 shows that the strongest signals are diffracted from the transmitter hallway corner and thereby arrive at the receiver near 180 degrees. Figure 5.14 and fig. 5.15 give the results from positions 4 and 5, respectively. As the transmitter is moved farther from the intersection between the hallways, the waveguiding effect becomes more dominant. A comparison of all four NLOS measurements shows as the distance from the receiver to the transmitter hallway is increased, the angular spead of the signals around 0 and 180 degrees decreases. This waveguiding effect is due to the fact that any signals that do not propagate along the direction of the hallway are highly attenuated by multiple reflections and diffractions.

5.5 NLOS Measurements

NLOS classroom to hallway, and classroom to classroom measurements were made on the second floor of the EL building. Figure 5.16 (created according to research by Jared Bench) shows that the transmitter was located in a classroom, while the receiver was located in a different classroom and moved to positions hallway positions detailed in the Appendix. The arrows show the orientation used for each receiver location. Since for NLOS propagation environments, the received signal power will be significantly spread in both time and angle,

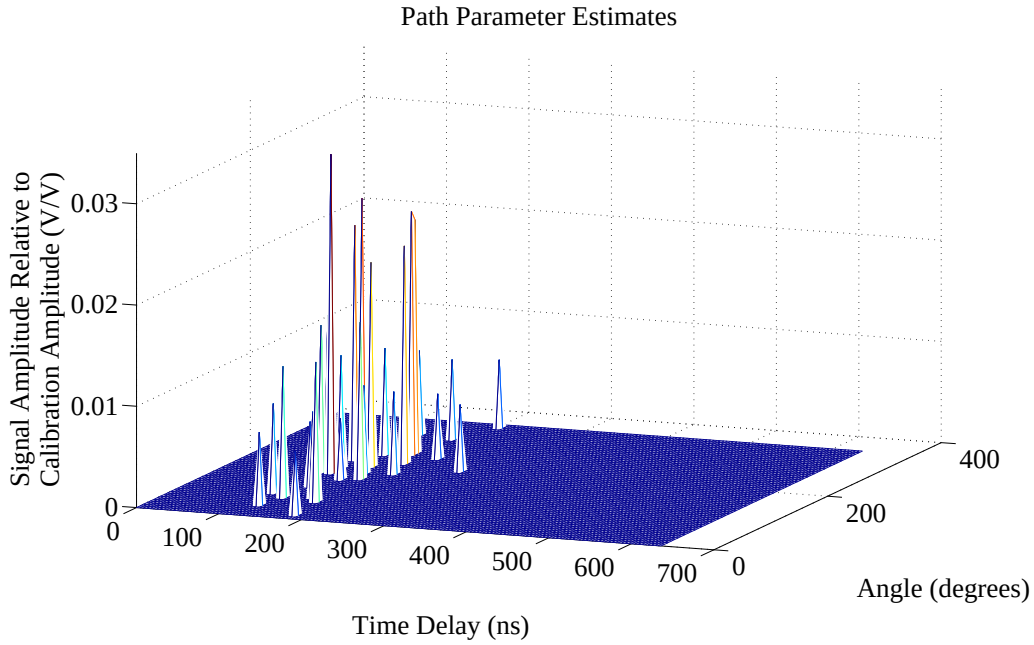

Fig. 5.13: 4^{th} floor NLOS measurement 3.

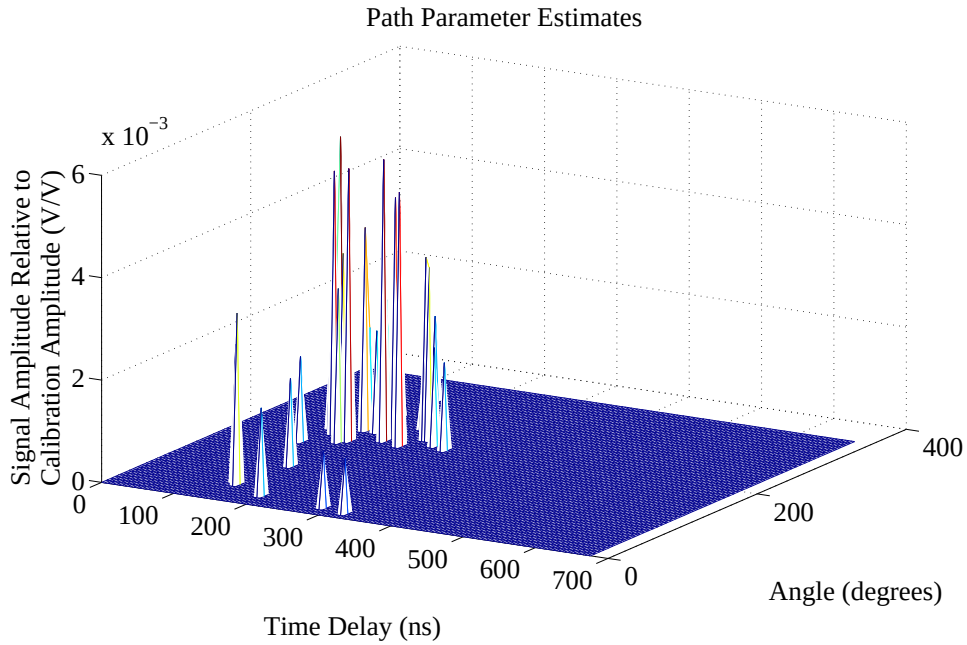

Fig. 5.14: 4^{th} floor NLOS measurement 4.

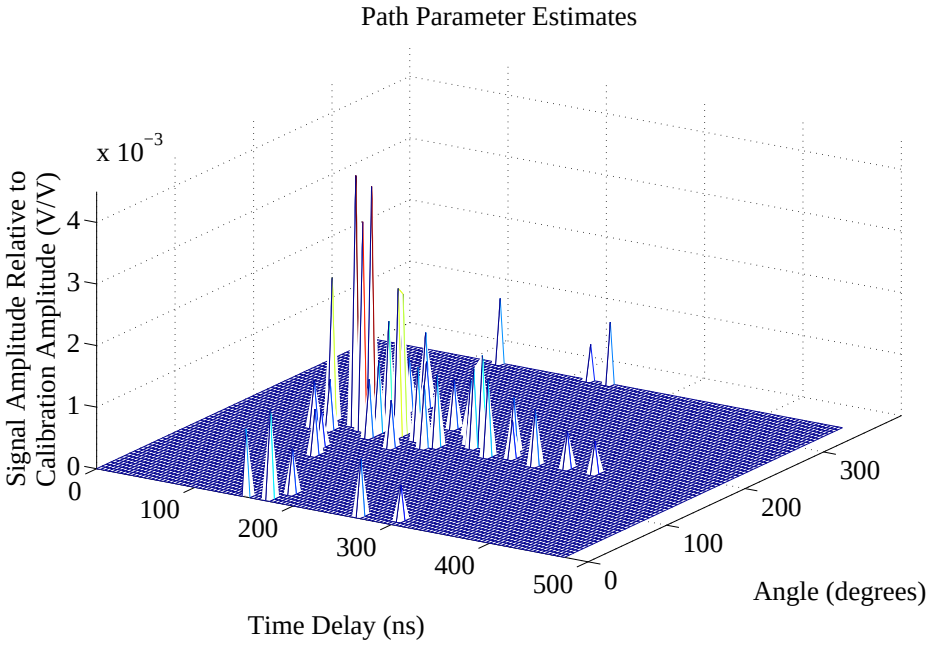

Fig. 5.15: 4^{th} floor NLOS measurement 5.

many iterations of the algorithm are required. Furthermore, since it is likely that many of the signals will arrive closely spaced in either time or angle, and more than L iterations will be needed to determine the unbiased path parameters. As discussed in Chapter 4, without a reduction in resolution or SNR, the time required to estimated enough paths becomes impractical. In many NLOS cases the SNR is already reduced to below 0 dB causing the algorithm to incorrectly estimate the path parameters. For these reasons it is difficult to draw set conclusions on the accuracy of the NLOS measurement results. In each NLOS measurement case descibed 60 iterations were performed. The results cannot be used to determine exact path parameter estimates, but may be used to determine the delay and AOA of the majority of the signal power.

The first NLOS measurement was made with the receiver located two classrooms to the north of the transmitter. Both classrooms have tables aligned in rows running east to west. Pictures of each classroom are given in the Appendix. On the front (south side) of both rooms, there is a 3 meters wide space that runs east to west along the length of the classroom without any tables, where the transmitter and receiver were located. Figure 5.17

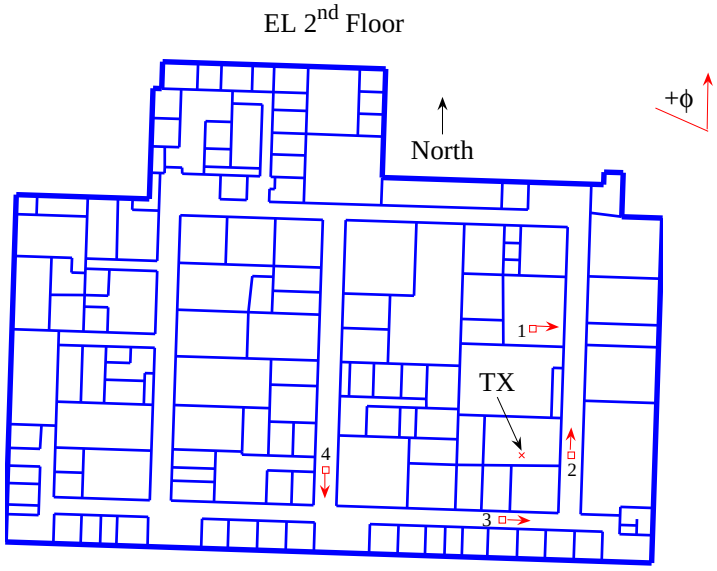

Fig. 5.16: Locations of EL NLOS classroom measurements.

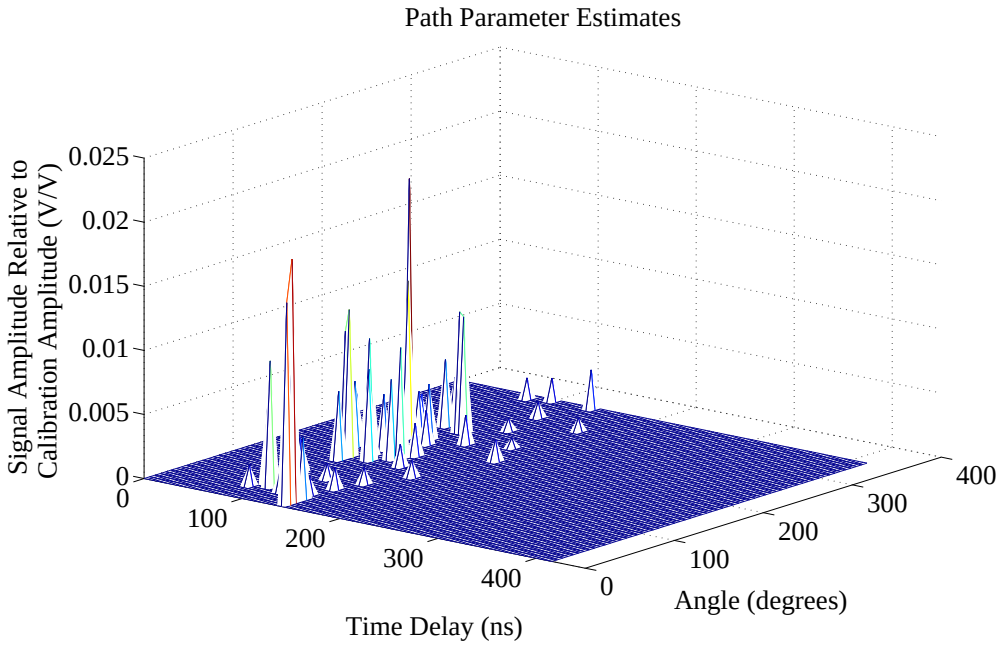

Fig. 5.17: Classroom-to-classroom propagation (Position 1).

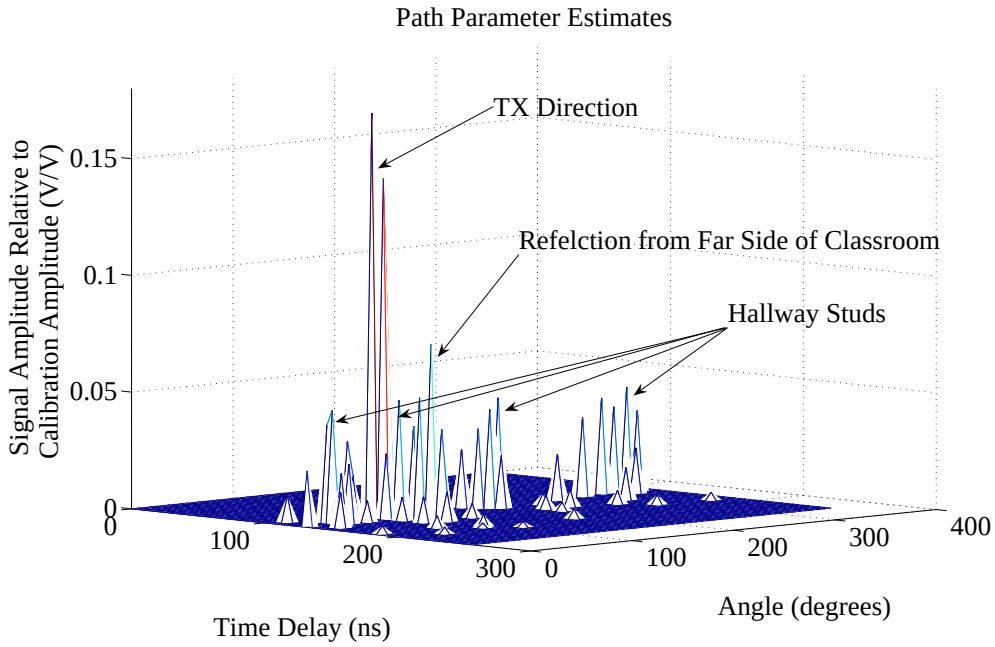

Fig. 5.18: Classroom-to-hallway propagation (Position 2).

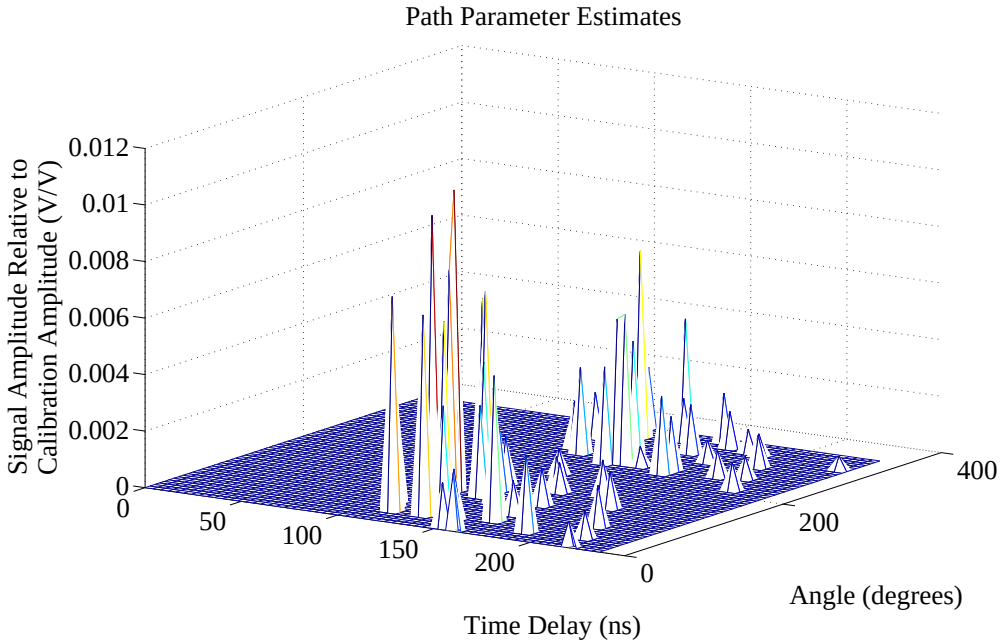

Fig. 5.19: Classroom-to-hallway propagation (Position 3).

shows the parameter estimates. The strongest signal arrives at about 210 degrees, while the transmitter is located at 270 degrees. The second strongest signal arrives at 0 degrees. It is unlikely that a strong signal component actually arrives at 0 degrees. In this case, the error can most likely be attributed to low SNR.

The results for measurement position 2 are shown in fig. 5.18. The transmitter was located at 90 degrees with respect to the array, at a distance of about six meters. Because of a much higher SNR, the results correctly show that the strongest signal arrives at 90 degrees. It also shows that there are echoes also at 90 degrees that arrive 32 ns after the direct path signal which correspond well with a reflection from the other side of the classroom. Many other signals arrive about 8-16 ns after the direct path signal. These signals are spread throughout many angles and may likely be reflections from the interior studs in both sides of the hallway.

The results for measurement position 3 are shown in fig. 5.19. A cluster of signals arrive at the receiver from the direction of the transmitter which is about 80 degrees. Another significant cluster is found between 270 and 360 degrees. Because the second cluster is delayed in time with respect to the first, and the amplitudes are on average smaller than those of the first, it is likely that some of the path estimates in the second cluster are reflections from objects in the offices to the north of the receiver hallway. For measurement position 4, only noise was estimated by the MLE.

Since only two to four snapshots were used at each NLOS location, there was no significant increase in effective SNR, and the algorithm was not able to estimate the unbiased parameters in NLOS cases. Furthermore, too much processing time was required to ensure that enough iterations were performed. An increase in SNR and more iterations of the MLE algorithm would provide more useful results in NLOS measruments.

Chapter 6

Conclusion

Emerging wireless communication systems such as smart antennas, SDMA, and MIMO systems require models to predict the spatial diversity of the the wireless channel. Temporal and angular dispersion information are needed to create accurate models to assist in planning modern wireless systems. This work describes a channel sounder that was built and used to estimate multipath channel parameters in both the temporal and angular domains. The sounder used a 2.45 GHz carrier modulated by a 100 MHz bandwidth maximal length pn sequence as the transmitted signal. The receiver consisted of a 12-element switched circular array with a 13^{th} element located at the array center that was used to detect a reference signal. It was discovered during the development of the sounder that mutual coupling effects and the shadowing of one element by another prevented the use of standard DOA algorithms that are based on ideal array responses. The well-known maximum likelihood estimation algorithm was adapted to estimate the angle and time of arrival of multipath signals based on array calibration. Calibration matrices were formed by measuring a single arrival at 60 equally spaced angles in the azimuth plane. Based on the maximum likelihood principle, the estimated multipath parameters were determined from the set of calibrations matrices that most likely formed the received measurement.

Simulations of closely spaced multiple signal arrivals were performed based on the measured calibration matrices. The resolution of a first order maximum likelihood estimation is about 40 degrees and 20 ns. A super-resolution algorithm was developed that iteratively increased the model order. As the model order increased, invalid estimates were replaced by the true values. In simulations without noise the algorithm was able to resolve signals that were separated by 6 degrees in the spatial domain and 4 ns in the temporal domain. As the noise increased, good estimates were still found for all signals sufficiently spaced

in time and angle of arrival. In simulations with low SNR, closely spaced signals were no longer resolvable.

Measurements to detect multipath parameters were made in the engineering complex on campus at Utah State University. For LOS hallway scenarios, the signal components arriving along the direction of the hallways were accurately detected. False estimates were made at the same time as other signal arrivals, but spread throughout various angles. These false estimates were easily detected in LOS measurements. For NLOS measurements, it was difficult to discriminate between actual signal arrivals and false estimates.

It was discovered after the majority of the measurements had been made that small positional displacements had occured to some elements of the array, and to other RF components in the receiver that degraded the accuracy of the measurements. The receiver was rebuilt and all components were securely mounted and tightened to minimize positional errors. A second calibration measurement was made. It was determined that the most likely causes of false estimates were imperfections in the calibration measurements and the fact that the calibration basis functions are not orthogonal and thereby introduce bias into signal estimates if too many iterations are performed.

A number of refinements can be made to the system that would improve its accuracy. In the current configuration, the array is divided into banks of antennas, where each bank consists of the reference antenna and three adjacent antennas. An improved method that does not favor any particular direction would be to stagger the antennas measured at each bank. Table 6.1 shows one possible bank/antenna arrangement.

Another area for future research would be to make mulitiple calibration measurements to determine the repeatability of the calibration. A more suitable location for the calibrations where signal reflections from objects, both beyond the receiver and behind the transmitter, are more attenuated could be located.

Better results will be found if the SNR of the measurements is increased. The received signal power can be increased by cascading multiple LNA's in each receiver channel, but not without some increase in noise power. A more efficient method would be to use a

Table 6.1: A possible bank arangement improvement.

Oscilloscope Channel	Bank 1 Antenna	Bank 2 Antenna	Bank 3 Antenna	Bank 4 Antenna
1	Ref	Ref	Ref	Ref
2	1	2	3	4
3	5	6	7	8
4	9	10	11	12

higher power amplifier at the transmit end. Furthermore, increasing the number of sample snapshots at each measurement location should increase the SNR.

Finally, the results of future measurements can be used to determine the multipath parameter statistics and compare them with the published results from similar studies [8], [9], [17]. The system is currently being used to compare measurements made in indoor channels with the results of site-specific ray-tracing simulations.

References

[1] M. A. Jensen and J. W. Wallace, "A review of antennas and propagation for MIMO wireless applications," *IEEE Transactions on Antennas and Propagation*, vol. 52, pp. 2810–2824, Nov. 2004.

[2] J. Fuhl, J. P. Rossi, and E. Bonek, "High-resolution 3-D direction-of-arrival determination for urban mobile radio," *IEEE Transactions on Antennas and Propagation*, vol. 45, pp. 672–682, Apr. 1997.

[3] R. D. Tingley and K. Pahlevan, "Space-time measurement of indoor radio propagation," *IEEE Transactions on Instrumentation and Measurement*, vol. 50, pp. 22–31, Feb. 2001.

[4] K. Kalliola, H. Laitinen, L. I. Vaskelainen, and P. Vainikainen, "Real-time 3D spatial dual-polarized measurement of wide-band radio channel at mobile station," *IEEE Transactions on Instrumentation and Measurement*, vol. 49, pp. 439–448, Apr. 2000.

[5] J.-P. Rossi, J.-P. Barbot, and A. J. Levy, "Theory and measurement of the angle of arrival and time delay of UHF radiowaves using a ring array," *IEEE Transactions on Antennas and Propagation*, vol. 45, pp. 876–884, May 1997.

[6] W. G. Newhall, T. S. Rappaport, and D. G. Sweeney, "A spread spectrum sliding correlator system for propagation measurements," *RF Design*, pp. 40–54, Apr. 2000.

[7] D. Tholl, M. Fattouche, R. J. C. Bultitude, P. MelanGon, and H. Zaghloul, "A comparison of two radio propagation channel impulse response determination techniques," *IEEE Transaction on Antennas and Propagation*, vol. 41, pp. 515–517, Apr. 2003.

[8] H. Xu, V. Kukshya, and T. S. Rappaport, "Spatial and temporal characteristics of 60-GHz indoor channels," *IEEE Journal on Selected Areas in Communications*, vol. 20, pp. 620–629, Apr. 2002.

[9] Q. H. Spencer, B. D. Jeffs, M. A. Jensen, and A. L. Swindlehurst, "Modeling the statistical time and angle of arrival characteristics of an indoor multipath channel," *IEEE Journal on Selected Areas in Communications*, vol. 18, pp. 347–360, Mar. 2000.

[10] J. Laurila, K. Kalliola, M. Toeltsch, K. Hugl, P. Vainikainen, and E. Bonek, "Wideband 3-D characterization of mobile radio channels in urban environment," *IEEE Transactions on Antennas and Propagation*, vol. 50, pp. 1–11, Jan. 2002.

[11] M. Wax and J. Sheinvald, "Direction finding of coherent signals via spatial smoothing for uniform circular arrays," *IEEE Transaction on Antennas and Propagation*, vol. 42, pp. 613–620, May 1994.

[12] B. H. Fleury, M. Tschudin, R. Heddergott, D. Dahlhaus, and K. I. Pedersen, "Channel parameter estimation in mobile radio environments using the SAGE algorithm," *IEEE Journal on Selected Areas in Communications*, vol. 17, pp. 434–450, Mar. 1999.

[13] M. Zeytinoglu and S. Foda, "Parallel implementation of high-resolution direction-finding algorithms with circular arrays," in *IEEE Pacific Rim Conference on Communications, Computers and Signal Processing*, May 9-10 1991.

[14] K. Kalliola, H. Laitinen, P. Vainikainen, M. Toeltsch, J. Laurila, and E. Bonek, "3-D double-directional radio channel characterization for urban macrocellular applications," *IEEE Transaction on Antennas and Propagation*, vol. 51, pp. 3122–3133, Nov. 2003.

[15] A. Kuchar, J.-P. Rossi, and E. Bonek, "Directional macro-cell channel characterization from urban measurements," *IEEE Transaction on Antennas and Propagation*, vol. 48, pp. 137–146, Feb. 2000.

[16] Y. L. C. de Jong and M. H. A. J. Herben, "High-resolution angle-of-arrival measurement of the mobile radio channel," *IEEE Transaction on Antennas and Propagation*, vol. 47, pp. 1677–1687, Nov. 1999.

[17] G. D. Durgin, V. Kukshya, and T. S. Rappaport, "Wideband measurements of angle and delay dispersion for outdoor and indoor peer-to-peer radio channels at 1920 MHz," *IEEE Transaction on Antennas and Propagation*, vol. 51, pp. 936–944, May 2003.

[18] J.-P. Barbot, P. Larzabal, and A. J. Levy, "Wideband indoor propagation channel direction of arrival measurements," in *First IEEE Signal Processing Workshop on Signal Processing Advances in Wireless Communications*, Apr. 1997.

[19] T. K. Moon and W. C. Stirling, *Mathematical Methods and Algorithms for Signal Processing*, ch. 12, pp. 542–567. Upper Saddle River, NJ: Prentice Hall, 2000.

[20] H. L. V. Trees, *Detection, Estimation, and Modulation Theory: Part I*, ch. 2, pp. 65–72. John Wiley and Sons, New York, 1968.

[21] H. Krim and M. Viberg, "Two decades of array signal processing research: The parameteric approach," *IEEE Signal Processing Magazine*, vol. 13, pp. 67–94, July 1996.

Appendix

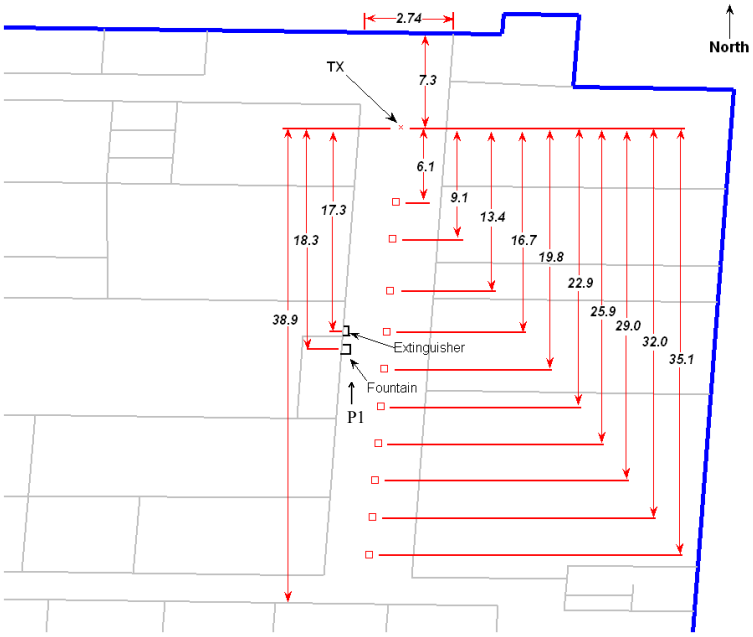

Fig. A.1: EL second floor hallway measurement distances.

Fig. A.2: Picture from location P1.

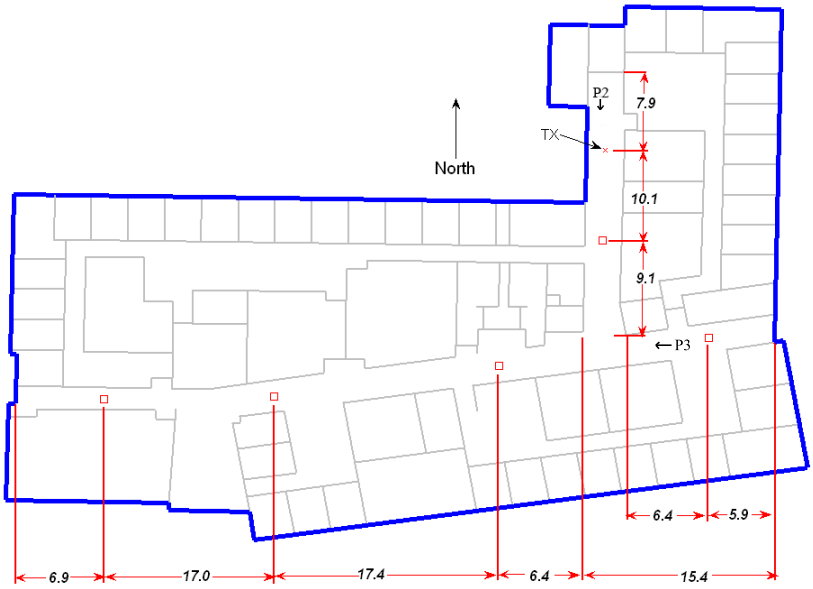

Fig. A.3: ENGR fourth floor measurement distances.

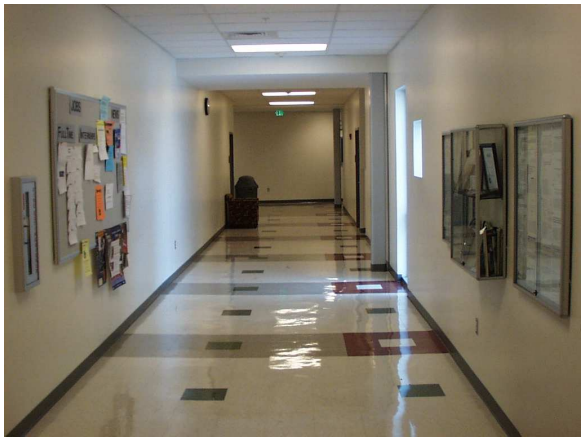

Fig. A.4: Picture from location P2.

Fig. A.5: Picture from location P3.

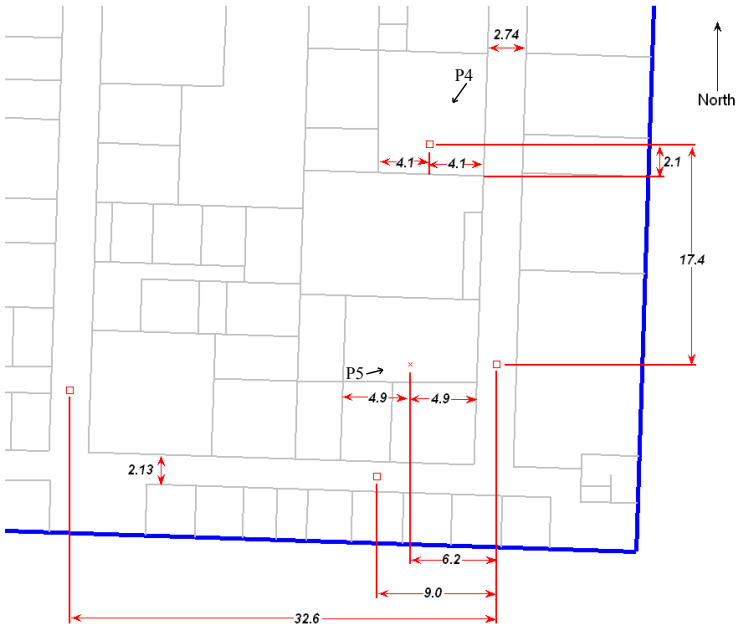

Fig. A.6: EL second floor classroom measurement distances.

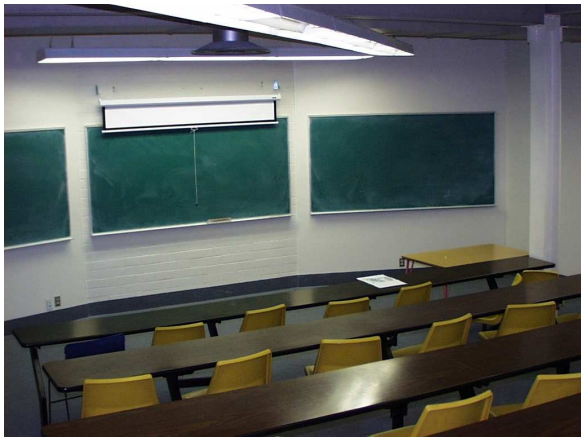

Fig. A.7: Picture from location P4.

Fig. A.8: Picture from location P5.

a